

# Global Sensitivity Analysis of Four Chamber Heart Hemodynamics Using Surrogate Models

Elias Karabelas, Stefano Longobardi, Jana Fuchsberger, Orod Razeghi, Cristobal Rodero, Marina Strocchi, Ronak Rajani, Gundolf Haase, Gernot Plank and Steven Niederer

**Abstract**—Computational Fluid Dynamics (CFD) is used to assist in designing artificial valves and planning procedures, focusing on local flow features. However, assessing the impact on overall cardiovascular function or predicting longer-term outcomes may require more comprehensive whole heart CFD models. Fitting such models to patient data requires numerous computationally expensive simulations, and depends on specific clinical measurements to constrain model parameters, hampering clinical adoption. Surrogate models can help to accelerate the fitting process while accounting for the added uncertainty. We create a validated patient-specific four-chamber heart CFD model based on the Navier-Stokes-Brinkman (NSB) equations and test Gaussian Process Emulators (GPEs) as a surrogate model for performing a variance-based global sensitivity analysis (GSA). GSA identified preload as the dominant driver of flow in both the right and left side of the heart, respectively. Left-right differences were seen in terms of vascular outflow resistances, with pulmonary artery resistance having a much larger impact on flow than aortic

resistance. Our results suggest that GPEs can be used to identify parameters in personalized whole heart CFD models, and highlight the importance of accurate preload measurements.

**Index Terms**—Fluid Dynamics, Biomedical Computing, Finite Element Analysis, Scientific computing, Gaussian processes

## I. INTRODUCTION

VALVULAR heart disease is a growing problem with limited pharmacological therapies [1]. Patients with valvular malfunctions are at high risk of developing cardiovascular diseases (CVD) [2]. Valve treatments rely on invasive surgery or catheter-based implanted valves [3]. Choosing the best option for each patient remains a challenge [4].

However, our understanding of how valvular diseases affect the heart and cardiovascular system as a whole remains incomplete. Mechanistic models [5] encapsulate our knowledge of physiology and the underlying fundamental laws of physics. They provide a framework to integrate experimental and clinical data, enabling the identification of mechanisms and/or the prediction of outcomes, even under unseen scenarios without the need for retraining [6]. Computational fluid dynamics (CFD) is routinely used for designing valves [7] and guiding implantation planning [8]. These simulations focus on modeling local blood flow across the valve and do not consider blood flow in the wider heart. Simulating blood flow in the whole heart can be important when estimating pressure gradients in the left ventricular outflow tract in transcatheter mitral valve implants (TMVI) [9], or when considering ventricle size in transcatheter aortic valve implants (TAVI) [10]. However, patient-specific simulations of blood flow in the whole heart requires parameters and boundary conditions to be tuned to an individual, requiring numerous expensive simulation. There is a need to reduce the computational cost of simulations and to focus simulations on tuning important parameters. Previous studies have performed local sensitivity analysis in simplified models, see for example [11], [12], however, these fail to provide an estimate of global and multi-factorial sensitivity. Identifying the key parameters that need to be personalized will both focus clinical measurements of key patient phenotypes and reduce the parameter space that needs to be explored to personalize the models.

The gold standard for modeling valves casts blood-valve interaction as a transient fluid–structure interaction (FSI)

S. Niederer acknowledges support from the UK Engineering and Physical Sciences Research Council (grant nos. EP/M012492/1, NS/A000049/1 and EP/P01268X/1), the British Heart Foundation (grant nos. PG/15/91/31812, PG/13/37/30280, SP/18/6/33805), US National Institutes of Health (grant no. NIH R01-HL152256), European Research Council (grant no. ERC PREDICT-HF 864055), Wellcome Trust (grant no. WT 203148/Z/16/Z) and Kings Health Partners London National Institute for Health Research (NIHR) Biomedical Research Centre, and UK HPC resources ARCHER.

G. Haase and G. Plank acknowledge support from grants nos. F3210-N18 and I2760-B30 from the Austrian Science Fund (FWF) and by BioTechMed-Graz (Grant No. Flagship Project: ILearnHeart).

C. Rodero acknowledges support from the European Union's Horizon 2020 Research and innovation programme under the Marie Skłodowska-Curie Grant Agreement No 764738.

We further acknowledge support by NAWI Graz and by the PRACE project "71138: Image-based Learning in Predictive Personalized Models of Total Heart Function" for awarding us access to the Austrian HPC resources VSC4.

E. Karabelas, J. Fuchsberger, and G. Haase are with the Department of Mathematics and Scientific Computing, University of Graz, Graz, AT. S. Longobardi, C. Rodero, M. Strocchi, and S. Niederer (corresponding author) are with the Cardiac Electromechanics Research Group, School of Biomedical Engineering and Imaging Sciences, King's College London, London, UK (e-mail: steven.niederer@kcl.ac.uk)

O. Razeghi is with the Research IT Services Department, University College London, London, UK

R. Rajani is with the Department of Adult Echocardiography, Guy's and St Thomas' Hospitals NHS Foundation Trust, London, UK

G. Plank is with the Gottfried Schatz Research Center (for Cell Signaling, Metabolism and Aging), Division Biophysics, Medical University of Graz, Graz, AT

E. Karabelas and S. Longobardi contributed equally to this paper.

**This work has been submitted to the IEEE for possible publication. Copyright may be transferred without notice, after which this version may no longer be accessible.**

problem. Recent advances [13]–[15] show the potential of fully coupled FSI models. However, computational costs and patient-specific parametrization [16] still pose major obstacles, hindering a swift clinical translation. Immersed boundary methods (IBM) [17] have proven to be a promising alternative, combining computational efficiency, ease of implementation, and numerical stability [18], especially when applied to heart valve modeling [19]–[21].

In this study we create and validate a patient-specific model of blood flow across the four chambers of the heart using the residual-based variational multiscale formulation (RBVMS) [22] of the arbitrary Lagrangian-Eulerian Navier-Stokes-Brinkman equations (ALE-NSB) [23], [24]. We test the ability of machine learning-based GPEs, which approximate the model and estimate the uncertainty in the approximation, to provide a low-cost surrogate for the full physics-based model. Using GPEs, we perform a variance-based GSA over parameters governing flow in the left and right heart to determine which of those are most important and need to be accurately personalized for patient-specific predictions.

## II. METHODS

### A. Ethics Declaration

This study uses a fully anonymized data set collected at Guy’s and St Thomas’ Hospital, London, United Kingdom, as part of standard of care.

### B. Data Acquisition

The patient received a ECG-gated cardiac CT angiography. Clinically indicated MDCT was performed as the standard of care using the hospital’s 3<sup>rd</sup> generation dual-source CT system (SOMATOM Force, Siemens Healthcare, Forchheim, Germany) equipped with an integrated high-resolution detector (Stellar Technology, Siemens). Intravenous contrast (Omnipaque, GE Healthcare, Princeton, NJ) was administered using power injector ( $5 \text{ mL s}^{-1}$ ) via the ante-cubital vein followed by saline flush (60–90 mL total contrast volume). Descending aorta contrast-triggered (100 Hounsfield units [HU] at 120kVp), electrocardiogram (ECG)-gated formal CT data acquisition was begun on reaching this threshold with a 10 second delay. CT parameters include a slice collimation of  $192 \times 0.6 \text{ mm}$ , gantry rotation time of 250 ms, pitch of 3.2. Automated tube current modulation was performed using a reference tube current–time product of 400 mAs and using automated attenuation-based tube voltage selection with a reference tube potential of 120 kVp. Initial retrospective ECG-gated scans were reconstructed in 5% phase increments throughout the cardiac cycle using iterative reconstruction, slice thickness of 0.6 mm and an increment of 0.4 mm. Patient data is summarized in Table I.

### C. Model Generation

Cardiac anatomy was automatically segmented from the CT DICOM images [25]–[27], to provide labels for all cardiac chambers and major vessels (Figure 1a). Additional post processing was performed using Seg3D<sup>1</sup> and Slicer<sup>2</sup> to obtain

TABLE I: Patient data.

Parameter	Value
Left ventricular ejection fraction (LVEF)	34 %
Left ventricular end diastolic volume (LVEDV)	414 mL
Left ventricular end systolic volume (LVESV)	274 mL
Hear rate (HR)	83 bpm
Cardiac output (CO)	11.62 L min <sup>-1</sup>
Systolic cuff pressure ( $P_{\text{sys}}^{\text{cuff}}$ )	97 mmHg
Diastolic cuff pressure ( $P_{\text{dia}}^{\text{cuff}}$ )	57 mmHg
Gender	male
Age	74

16 labels comprising left ventricle (LV), right ventricle (RV), left atrium (LA), right atrium (RA), aorta (AO), and pulmonary artery (PA) blood pools as well as labels encoding the locations of aortic valve (AV), mitral valve (MV), pulmonary valve (PV) and tricuspid valve (TV). Valve labels were automatically generated as thin voxel regions between compartment regions see Figure 1e). Multilabel segmentations were used to create an unstructured finite element surface mesh using CGAL<sup>3</sup>, which served as input for the unstructured volumetric mesh generation, including three prismatic boundary layers, using the software package Meshtool [28] (see Figure 1b). Cardiac kinematics was extracted over one cardiac cycle by non-rigid registration, using the sparse free-form deformation (SFFD) technique [29] that extends the classic FFD approach and recovers smoother displacement fields [30], [31].

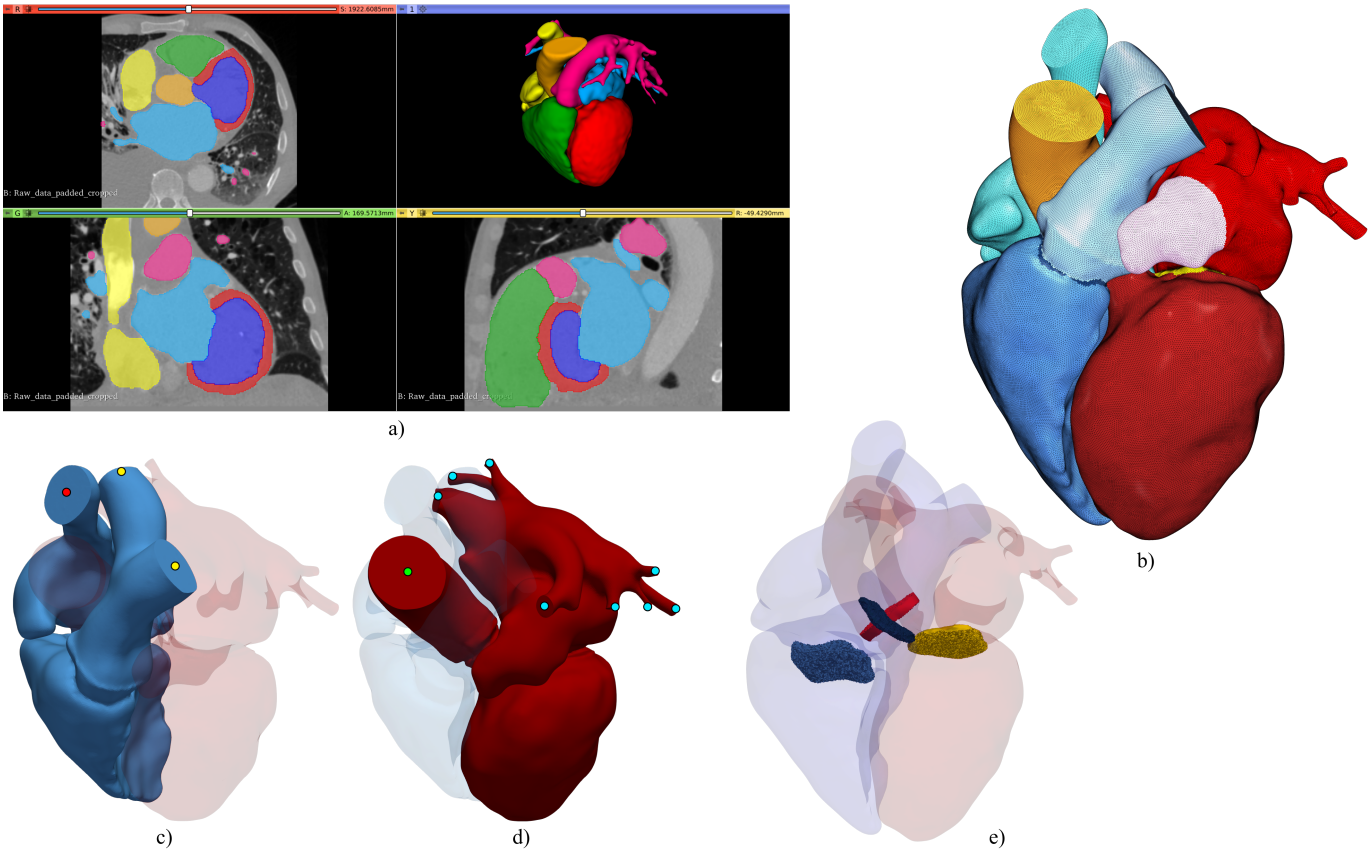
### D. Computational Methods & Simulation

Image derived kinematics was used as input to drive the CFD model of whole-heart hemodynamics. With prescribed motion, blood flow in the left and right heart can be simulated independently. Assuming Newtonian blood flow, hemodynamics is modeled with an arbitrary Lagrangian-Eulerian (ALE) formulation of the Navier-Stokes equations [32], [33]. The effect of heart valves upon blood flow is taken into account by including an ad-hoc extension to the ALE-Navier-Stokes-Brinkman (ALE-NSB) equations with an added Darcy drag term penalizing flow in the areas covered by the valves [23], [24], [34], [35]. Extensions required for moving domains are explained in more detail in Supplement S.I. Computational domains labeled as valves are parameterized by a penalty parameter  $\kappa_*$ , modeling vanishing permeability, with \* denoting any of the four heart valves, AV, MV, PV, TV, and the duration  $\text{dur}_*$  (see Figure 2 for an illustration) of valve opening and closing. A RBVMS discretization is used [22], adapted to the ALE-NSB equations. A generalized- $\alpha$  integrator [36] with  $\rho_\infty = 0.2$  is employed for time discretization and the arising non-linear systems are solved with an inexact Newton-Raphson method [37]. Domain motion was extended into the interior of the blood pool using a linear elastic model optimized for retaining finite element quality. Dirichlet displacement boundary conditions are used at the blood pool walls enforcing a velocity matching the time derivative of the registered cardiac motion. On the arterial outlets (aorta and pulmonary artery) we used 0D three element Windkessel models [38]. Windkessel parameters of systemic circulation comprising characteristic impedance,

<sup>1</sup><https://www.sci.utah.edu/cibc-software/seg3d.html>

<sup>2</sup><https://www.slicer.org/>

<sup>3</sup><https://www.cgal.org/>



**Fig. 1:** Whole heart model generation workflow. Shown are a) the pre-final segmentation in *Slicer* before automatically adding valve regions, b) the final multi-label mesh, the outflow boundaries for c) the right heart, marked by red and yellow circles, and d) the left heart, marked by green and blue circles, and e) the automatically generated valve regions.

$Z_{WK}$ , resistance  $R_{WK}$  and compliance  $C_{WK}$  were determined from cuff pressure measurements [39], [40]. This resulted in  $R_{WK} = 49.89 \text{ kPa ms mL}^{-1}$ . Values for  $Z_{WK}$  and  $C_{WK}$  were determined as  $0.05R_{WK}$  and  $C_{WK} = \frac{HR}{R_{WK}}$  respectively. As no pressure measurements were available for the right heart, Windkessel parameters for the pulmonary circulation were estimated by assuming a default value of 14 mmHg for mean pulmonary artery pressure [41] and estimating Windkessel parameters from this value. RV cardiac output was estimated from its end diastolic and end systolic volume, with the latter estimated from the volume transients in Figure 3. At the other outlets pressures  $p_{LA} = 10 \text{ mmHg}$  and  $p_{RA} = 5 \text{ mmHg}$  were prescribed. The location of all outlets are illustrated in Figure 1c) and Figure 1d). For numerical stability the directional do-nothing outflow stabilization [42] was used.

### E. Global Sensitivity Analysis

To quantify the impact of input parameters on the total variance of output features global sensitivity analysis (GSA) using *Gaussian process emulation* (GPE) was employed to replace the highly non-linear computationally expensive map from parameters to features with a fast-evaluating, probabilistic surrogate map. We selected  $D$  parameters and  $M$  characteristic output features for the studied model. GPEs were trained following [43]. Briefly, we used a  $\approx 10D$  sized sample drawn from a Latin hypercube design in the  $D$ -dimensional parameter space

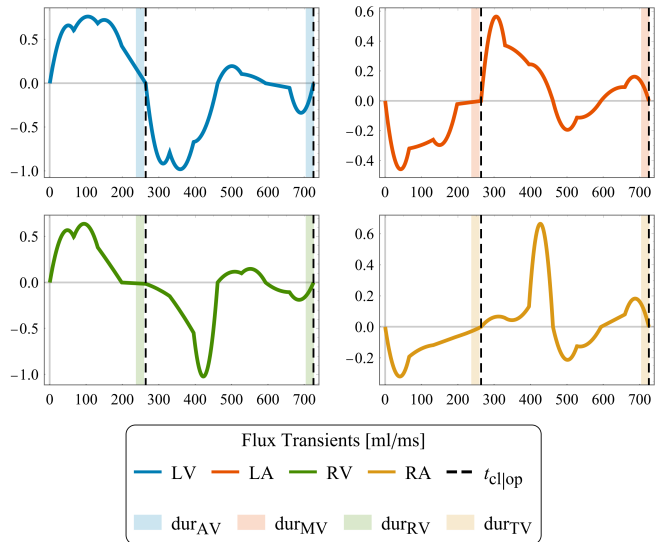


**Fig. 2:** Fluxes computed from volume transients of Figure 3. Dashed lines indicated timings of valves switching, with opaque bars indicating the duration of switching.

with initial ranges given by  $\pm 25\%$  perturbation around the baseline values. Model simulations were carried out for each of these parameter sets and the successfully completed simulations

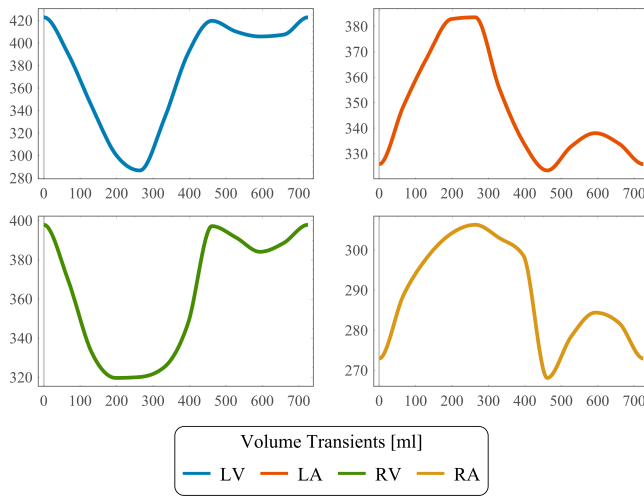


Fig. 3: Volume transients extracted from the registered mesh motion of LV, RV, LA and RA blood pool.

were collected to build the training dataset. Simulations where CFD simulation failed to converge were discarded. GPEs were defined as the sum of a deterministic mean function and a stochastic process [44] while the stochastic process is a centered zero-mean Gaussian process with stationary Matérn covariance function [45]. The model likelihood was taken to be Gaussian, i.e. the learning sample observations are modeled to be affected by an additive, independent and identically distributed noise.

## F. Computational Framework

1) *Computational Fluid Dynamics*: The discretized and linearized block system of the ALE-NSB equations was solved for each Newton–Raphson iteration and every time step. A flexible generalized minimal residual method (fGMRES) and efficient preconditioning based on the libraries PETSc<sup>4</sup> and hypre/BoomerAMG<sup>5</sup> were employed. CFD model and calculation of residence times have been implemented in an extension of the Cardiac Arrhythmia Research Package (carpentry) [46]. Parallel performance and scalability of carpentry has been previously investigated in [39], [47]. Details on numerical aspects are provided in Supplement S.I.C.

2) *GPE Training*: All the GPE’s (hyper)parameters were jointly optimized by maximization of the model log-marginal likelihood using GPERks emulation tool<sup>6</sup> based on the GPyTorch Python library<sup>7</sup>. Univariate GPEs were trained to predict each output feature using a 5-fold cross-validation process. GPEs’ accuracy was evaluated using the average  $R^2$ -score across the obtained scores when testing the emulators on the respective left-out parts of the dataset. The so trained GPEs were used as emulators for the global sensitivity analysis. Model outputs’ sensitivity to parameters was characterized by Sobol’ first-order  $S_1$  and total effects  $S_T$  [48].

<sup>4</sup><https://www.mcs.anl.gov/petsc/>

<sup>5</sup><https://hypre.readthedocs.io/en/latest/index.html>

<sup>6</sup><https://github.com/stelong/GPERks>

<sup>7</sup><https://gpytorch.ai/>

## G. Data Analysis

Pressure gradients and differences as well as flow velocities were calculated by computing spatial averages over spherical regions chosen as observation sites, see Figure 5b. Output features used for training were calculated from derived quantities by temporal averaging, or taking the temporal maximum over the whole cardiac cycle.

## III. RESULTS

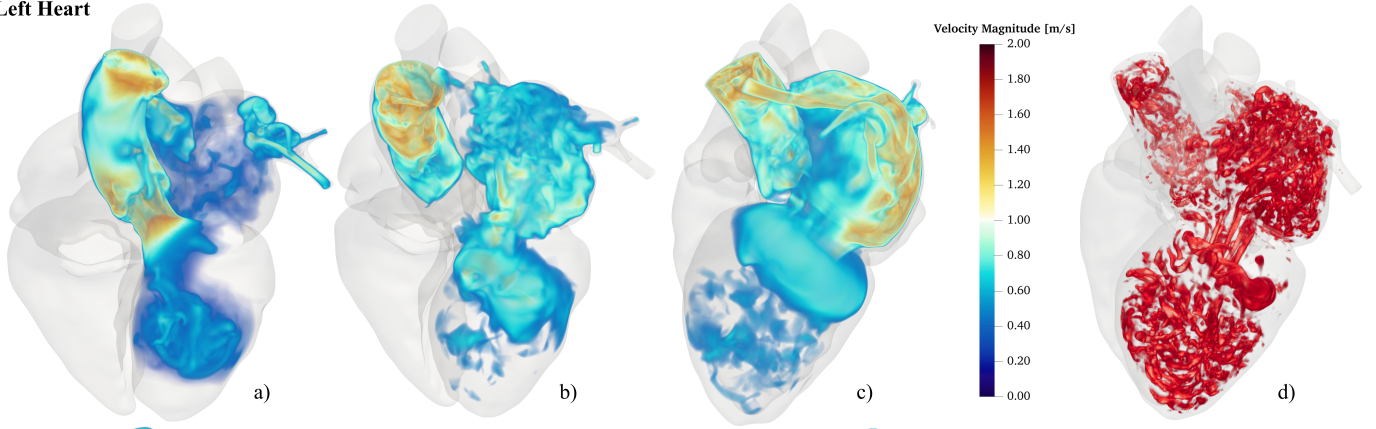
### A. Simulation

Four heartbeats were simulated at a time step of  $\Delta t = 0.3625$  ms resulting in 16000 time steps. Simulations were carried out on the *Vienna Scientific Cluster 4* (VSC4) using 1152 MPI processes and 672 MPI processes, with an average run time per time step of 18s and 9s and a total run time of 80h and 40h for left and right heart simulations, respectively. Volume renderings of the velocity magnitude at various time instances are shown in Figure 4. The large-scale flow characteristics in both ventricles is the formation of an asymmetric vortex ring (Figure 4c) and Figure 4e)) next to the MV and TV traveling towards the apex, also apparent in the visualization of the strain-normalized  $Q$  criterion in Figure 4d) and Figure 4h). As expected, jet formation is witnessed at the opening of the heart valves, see rightmost subfigures of Figure 4. Furthermore, flow in the AO shows strong non-laminar behavior and increased flow speeds can be observed in the upper areas of the LA. A video showing the final heartbeat is available as supplement.

### B. Global Sensitivity Analysis Using Surrogate Models

We performed a GSA for both sides of the heart as outlined in subsection II-E. First, we used  $D = 6$  parameters (summarized in Table II) as key regulators of our left heart model, and we characterized the model behavior at a specific set of parameters using  $M = 16$  features with notation and baseline values summarized in Table III. More specific, we used the following output features: mean systolic pressure gradient over aortic valve (AV),  $\Delta p_{AV}$ , and mean diastolic pressure gradient over mitral valve (MV),  $\Delta p_{MV}$ , as defined in [49]; mean pressure difference between four landmark points in the LA and MV,  $\Delta p_{LMV1,2,3,4}$ ; mean pressure difference between apex and MV,  $\Delta p_{AMV}$ ; mean pressure difference between apex and AV,  $\Delta p_{AAV}$ ; mean pressure difference between AV and MV,  $\Delta p_{AVMV}$ ; mean pressure gradient over PV,  $\Delta p_{PV}$ ; mean pressure gradient over TV,  $\Delta p_{TV}$ ; mean pressure difference between four landmark points in the RA and TV,  $\Delta p_{RTV1,2,3}$ ; mean kinetic energy LV,  $E_{k,LV}$ ; mean kinetic energy AO,  $E_{k,AO}$ ; mean kinetic energy LA,  $E_{k,LA}$ ; mean kinetic energy RV,  $E_{k,RV}$ ; mean kinetic energy PV,  $E_{k,PV}$ ; mean kinetic energy RA,  $E_{k,RA}$ ; average residence time, LV  $RT_{LV}$ ; average residence time, RV  $RT_{RV}$ ; average residence time, left atrial appendage (LAAPP)  $RT_{APP}$ ; maximal velocity magnitude over AV,  $\max v_{AV}$ , MV,  $\max v_{MV}$ , PV,  $\max v_{PV}$ , and TV,  $\max v_{TV}$ . Residence times were calculated using an continuum approach described in [50] solved with the flux corrected transport finite element method (FCT-FEM) [51] adapted to moving grids, see Supplement S.III.

## Left Heart



## Right Heart

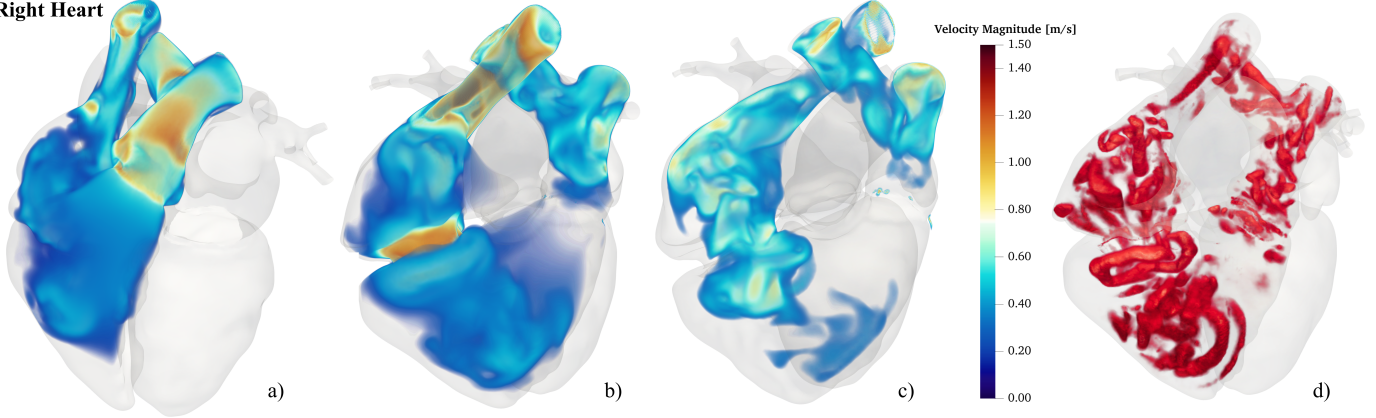


Fig. 4: CFD results show left (top panels) and right (bottom panels) heart blood flow at a) peak systole, b) end of systole, and c) peak diastole, and d) the strain normalized  $Q$  criterion at peak diastole.

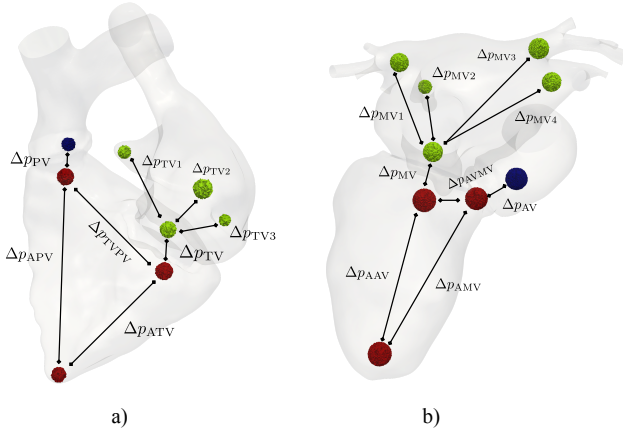


Fig. 5: Illustration of areas in the left and right heart used to compute pressure drops and differences respectively. A black line denotes that the pressure difference between those areas is calculated.

As described in subsection II-E, we used  $GPER_{ks}$  to incorporate full GPE's posterior distribution samples to estimate the first and total Sobol' indices  $S_1$  and  $S_T$  using Saltelli's method [52] with  $n = 10\,000$  samples drawn from each GPE. Sobol indices were calculated with the help of `SALib` python library [53]. Only GPEs having a mean  $R^2$  test score  $> 0.5$  were used for indices calculation. This resulted in excluding

TABLE II: Parameters identified for GPE training.

Parameter	Range	Description
$R_{WK,AO}$	$37.46 \frac{\text{kPa}\cdot\text{ms}}{\text{mL}}$ to $62.32 \frac{\text{kPa}\cdot\text{ms}}{\text{mL}}$	AO Windkessel resistance
$R_{WK,PA}$	$27.81 \frac{\text{kPa}\cdot\text{ms}}{\text{mL}}$ to $46.21 \frac{\text{kPa}\cdot\text{ms}}{\text{mL}}$	PA Windkessel resistance
$p_{LA}$	7.5 mmHg to 12.5 mmHg	LA outlet pressure
$p_{RA}$	3.5 mmHg to 8.5 mmHg	RA outlet pressure
$\kappa_{AV}$	$1 \times 10^{-5}$ to $1 \times 10^{-9}$	AV penalization parameter
$\kappa_{MV}$	$1 \times 10^{-5}$ to $1 \times 10^{-9}$	MV penalization parameter
$\text{dur}_*$	11.25 ms to 18.75 ms	Valve transition times with $*$ $\in \{AV, MV, PV, TV\}$

features  $\max_{VMV}$ ,  $\Delta p_{MV2}$ ,  $\Delta p_{MV3}$ , and  $\Delta p_{AMV}$  from the analysis. Parameters with resulting indices below 0.01 were considered to have no/negligible effect. The resulting indices are summarized as heat-maps in Figure 6a). From GSA we concluded that the penalization parameters  $\kappa_{AV}$ , and  $\kappa_{MV}$  have no or negligible effect and feature  $p_{LA}$  has a strong effect. The same procedure was carried out for the right bloodpool model with penalization parameters  $\kappa_*$  removed from the training phase due to negligible influence. We chose similar output features summarized in Table III. Results are summarized in Figure 6b) showing a strong effect of  $p_{RA}$  and  $R_{WK}$ .

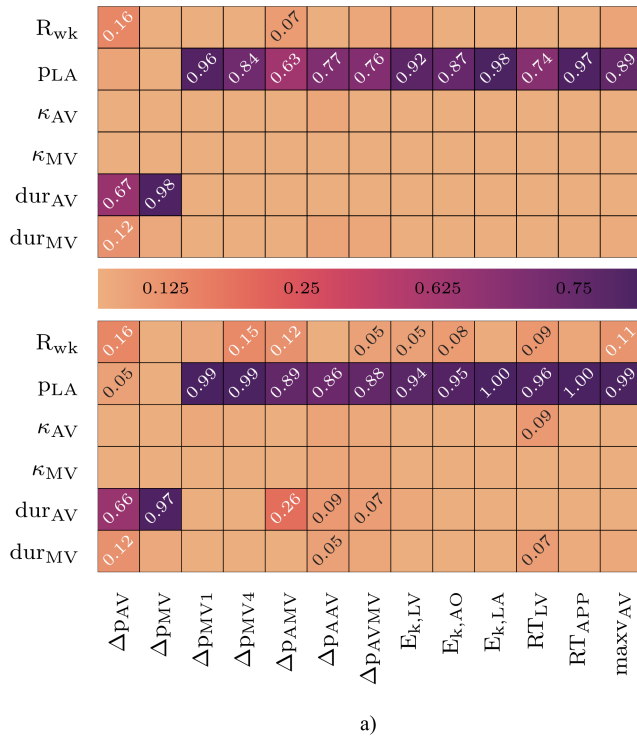
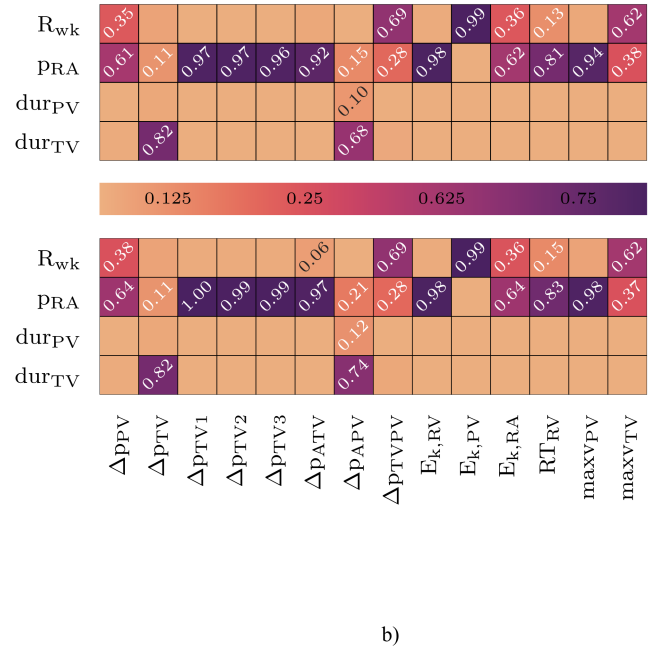
$S_1$  (top) and  $S_T$  (bottom) $S_1$  (top) and  $S_T$  (bottom)

Fig. 6: Heat maps of first and total order Sobol indices for the a) left heart and b) right heart GSA.

**TABLE III:** Output features for GPE training with reference values extracted from CFD simulations. Reported are temporal means, except for velocities reported as temporal maxima. Clinical measurements if reported are given as means of three measurements.

Parameter	<i>in silico</i> Reference Value	Clinical Measurements
$\Delta p_{AV}$	4.61 mmHg	5.0 mmHg
$\Delta p_{MV}$	2.71 mmHg	2.38 mmHg
$\Delta p_{MV1,2,3,4}$	-0.0106	
	0.225	
	0.183 mmHg	
	-0.0025	
$\Delta p_{AMV}$	1.732 mmHg	
$\Delta p_{AAV}$	1.60 mmHg	
$\Delta p_{AVMV}$	0.21 mmHg	
$\Delta p_{PV}$	2.35 mmHg	3.0 mmHg
$\Delta p_{TV}$	5.73 mmHg	47.0 mmHg
$\Delta p_{TV1,2,3}$	0.204	
	0.342 mmHg	
$E_{k,LV}$	16.71 mJ	
$E_{k,AO}$	22.59 mJ	
$E_{k,LA}$	23.33 mJ	
$E_{k,RV}$	3.65 mJ	
$E_{k,PV}$	5.51 mJ	
$E_{k,RA}$	9.59 mJ	
$RT_{LV}$	0.811 s	
$RT_{APP}$	0.854 s	
$RT_{RV}$	0.91 s	
$max_{V_{AV}}$	1.13 m s <sup>-1</sup>	1.15 m s <sup>-1</sup>
$max_{V_{MV}}$	0.73 m s <sup>-1</sup>	0.81 m s <sup>-1</sup>
$max_{V_{PV}}$	0.71 m s <sup>-1</sup>	0.814 m s <sup>-1</sup>
$max_{V_{TV}}$	0.57 m s <sup>-1</sup>	3.43 m s <sup>-1</sup>

#### IV. DISCUSSION

Being able to identify key parameters and regulators in a hemodynamic CFD model of the human heart is paramount for personalization. However, personalization of four chamber CFD models is computationally expensive. Here we show that the use of ALE-NSB allows computationally tractable simulations, the GPE can be used to emulate most outputs, and that pre load is the key parameter in determining boundary driven four chamber heart CFD models. Our CFD simulations took between 10 h and 20 h per heart beat for the left or right side of the heart. This breaks down to an average wallclock time of  $\approx 11$  s for performing one nonlinear time step of the CFD simulator. Comparing our average wallclock times with other approaches, for instance 11 s reported in [54] using IBM, or 30 s - 50 s reported in [55] using a semi-implicit algorithm with higher order finite elements, or 50 s reported in [56] using a similar algorithm as in this manuscript, we find that our ALE-NSB method provides a competitive implementation putting us well into the forecasted optimal wallclock times for hemodynamic CFD simulations shown in [7].

Comparing with clinically measured data in Table III we saw good agreement for  $max_{V_{AV,MV,PV}}$  with relative error of  $\approx 2\%$ ,  $10\%$ , and  $13\%$  similarly for  $\Delta p_{AV,MV,PV}$  with relative error of  $\approx 8\%$ ,  $13\%$ , and  $24\%$ . Clinical data suggested a possible TV regurgitation. We did not aim to capture TV regurgitation in the simulations, and this likely explains the discrepancy in  $max_{V_{TV}}$  and  $\Delta p_{TV}$ .

There is growing interest in using reduced order models and

physics informed neural networks (PINNs) for accelerating or creating model surrogates [57]. Each method has its purpose, here we show that GPEs, which are both fast and provide an estimate of uncertainty can be used to emulate most, but not all, four chamber heart CFD simulation outputs using  $\approx 10$  simulations per parameter. To train our GPEs we used in total 180 CFD simulations comprising 4 heart beats each. Executing those simulations took approximately 7700 h of wallclock time on the HPC clusters VSC4 (AT) and ARCHER (UK). Using those data sets we performed the first GSA of model parameters for informing cavity driven flow. Training of the GPEs and running GSA took approximately 5 h. Running GSA without a surrogate model would have resulted in intractable amounts of CFD simulations highlighting the possible savings in computing time and resources.

Output features  $\max_{\text{VMV}}$ ,  $\Delta p_{\text{MV}2}$ , and  $\Delta p_{\text{MV}3}$  showed  $R^2$  test scores below 0.5. As the GPEs are based on nonlinear CFD simulations, it is hard to give a definite answer as to why those particular features were excluded. Possible explanations could be, underresolved CFD grids close to extraction points of the features, or lacking temporal resolution.

We identified the pre-load as a key variable in defining simulation clinical outputs, in both the atrial and ventricle flow in four chamber boundary driven flow simulations. This highlights the need to have an accurate estimate of pre-load when performing boundary driven CFD simulations. As blood flows from the atria to the ventricle and then out through the aorta (or pulmonary artery) the parameters that impact atrial flow will impact down stream flows. Conversely, the after-load properties only impact blood flow out of the ventricle and do not directly impact the atrial flow. This potentially explains the importance of pre-load over after-load in our simulations. Furthermore, we considered time averages over the complete heart beat. During systole, pressure signals are not sensitive to any of the input parameters. However, this changes in diastole and we provide an additional explanation in Supplement S.V.

It is important to note that our findings are for the specific case of boundary driven flow and do not reflect the relative importance of pre-load and after-load in patients, where after-load can feedback on ventricle function, and hence atrial filling, so may play a far greater role physiologically.

## V. CONCLUSION

In this work we presented full GSA based on GPE surrogate models for four chamber heart hemodynamics. We showed that modeling valves using a penalization approach is independent of numerical parameters. GSA revealed strong influences of left and right atrial pressure and medium influence of arterial and pulmonary arterial resistances. These results show the possibility and potential speedup using surrogate models to replace full-blown CFD models for human heart hemodynamics.

## REFERENCES

- [1] S. Coffey, B. Cox, and M. J. Williams, "Lack of progress in valvular heart disease in the pre-transcatheter aortic valve replacement era: Increasing deaths and minimal change in mortality rate over the past three decades," *American Heart Journal*, vol. 167, no. 4, pp. 562–567.e2, Apr. 2014. [Online]. Available: <https://doi.org/10.1016/j.ahj.2013.12.030>
- [2] H. Ritchie and M. Roser, "Causes of death," *Our World in Data*, 2018. [Online]. Available: <https://ourworldindata.org/causes-of-death>
- [3] A. S. Manolis, "Transcatheter aortic valve implantation economics: a grisly reality," *Annals of Cardiothoracic Surgery*, vol. 6, no. 5, pp. 516–523, Sep. 2017. [Online]. Available: <https://doi.org/10.21037/acs.2017.07.02>
- [4] H. Baumgartner, V. Falk *et al.*, "2017 ESC/EACTS guidelines for the management of valvular heart disease," *European Heart Journal*, vol. 38, no. 36, pp. 2739–2791, Aug. 2017. [Online]. Available: <https://doi.org/10.1093/eurheartj/ehx391>
- [5] S. A. Niederer, J. Lumens, and N. A. Trayanova, "Computational models in cardiology," *Nature Reviews Cardiology*, vol. 16, no. 2, pp. 100–111, Oct. 2018. [Online]. Available: <https://doi.org/10.1038/s41569-018-0104-y>
- [6] M. R. Davies, K. Wang *et al.*, "Recent developments in using mechanistic cardiac modelling for drug safety evaluation," *Drug Discovery Today*, vol. 21, no. 6, pp. 924–938, Jun. 2016. [Online]. Available: <https://doi.org/10.1016/j.drudis.2016.02.003>
- [7] R. Mittal, J. H. Seo *et al.*, "Computational modeling of cardiac hemodynamics: Current status and future outlook," *Journal of Computational Physics*, vol. 305, pp. 1065–1082, Jan. 2016. [Online]. Available: <https://doi.org/10.1016/j.jcp.2015.11.022>
- [8] J. Brouwer, L. Gheorghe *et al.*, "Insight on patient specific computer modeling of transcatheter aortic valve implantation in patients with bicuspid aortic valve disease," *Catheterization and Cardiovascular Interventions*, vol. 93, no. 6, pp. 1097–1105, Nov. 2018. [Online]. Available: <https://doi.org/10.1002/ccd.27990>
- [9] P. Blanke, C. Naoum *et al.*, "Predicting LVOT obstruction in transcatheter mitral valve implantation," *JACC: Cardiovascular Imaging*, vol. 10, no. 4, pp. 482–485, Apr. 2017. [Online]. Available: <https://doi.org/10.1016/j.jcmg.2016.01.005>
- [10] T. Saito, T. Inohara *et al.*, "Small left ventricle and clinical outcomes after transcatheter aortic valve replacement," *Journal of the American Heart Association*, vol. 10, no. 7, Apr. 2021. [Online]. Available: <https://doi.org/10.1161/jaha.120.019543>
- [11] L. M. Ellwein, H. T. Tran *et al.*, "Sensitivity analysis and model assessment: Mathematical models for arterial blood flow and blood pressure," *Cardiovascular Engineering*, vol. 8, no. 2, pp. 94–108, Dec. 2007. [Online]. Available: <https://doi.org/10.1007/s10558-007-9047-3>
- [12] G. García-Isla, A. L. Olivares *et al.*, "Sensitivity analysis of geometrical parameters to study haemodynamics and thrombus formation in the left atrial appendage," *International Journal for Numerical Methods in Biomedical Engineering*, vol. 34, no. 8, p. e3100, Jun. 2018. [Online]. Available: <https://doi.org/10.1002/cnm.3100>
- [13] M. Astorino, J.-F. Gerbeau *et al.*, "Fluid–structure interaction and multi-body contact: Application to aortic valves," *Computer Methods in Applied Mechanics and Engineering*, vol. 198, no. 45–46, pp. 3603–3612, Sep. 2009. [Online]. Available: <https://doi.org/10.1016/j.cma.2008.09.012>
- [14] J. F. Wenk, Z. Zhang *et al.*, "First finite element model of the left ventricle with mitral valve: Insights into ischemic mitral regurgitation," *The Annals of Thoracic Surgery*, vol. 89, no. 5, pp. 1546–1553, May 2010. [Online]. Available: <https://doi.org/10.1016/j.athoracsur.2010.02.036>
- [15] T. Terahara, K. Takizawa *et al.*, "Heart valve isogeometric sequentially-coupled FSI analysis with the space–time topology change method," *Computational Mechanics*, vol. 65, no. 4, pp. 1167–1187, Jan. 2020. [Online]. Available: <https://doi.org/10.1007/s00466-019-01813-0>
- [16] M. Stevanella, F. Maffessanti *et al.*, "Mitral valve patient-specific finite element modeling from cardiac MRI: Application to an annuloplasty procedure," *Cardiovascular Engineering and Technology*, vol. 2, no. 2, pp. 66–76, Jan. 2011. [Online]. Available: <https://doi.org/10.1007/s13239-010-0032-4>
- [17] C. S. Peskin, "Flow patterns around heart valves: A numerical method," *Journal of Computational Physics*, vol. 10, no. 2, pp. 252–271, Oct. 1972. [Online]. Available: [https://doi.org/10.1016/0021-9991\(72\)90065-4](https://doi.org/10.1016/0021-9991(72)90065-4)
- [18] R. Mittal and G. Iaccarino, "IMMERSED BOUNDARY METHODS," *Annual Review of Fluid Mechanics*, vol. 37, no. 1, pp. 239–261, Jan. 2005. [Online]. Available: <https://doi.org/10.1146/annurev.fluid.37.061903.175743>
- [19] M. Astorino, J. Hamers *et al.*, "A robust and efficient valve model based on resistive immersed surfaces," *International Journal for Numerical Methods in Biomedical Engineering*, vol. 28, no. 9, pp. 937–959, May 2012. [Online]. Available: <https://doi.org/10.1002/cnm.2474>
- [20] E. Votta, T. B. Le *et al.*, "Toward patient-specific simulations of cardiac valves: State-of-the-art and future directions," *Journal of Biomechanics*, vol. 46, no. 2, pp. 217–228, Jan. 2013. [Online]. Available: <https://doi.org/10.1016/j.jbiomech.2012.10.026>

- [21] C. Chnafa, S. Mendez, and F. Nicoud, "Image-based large-eddy simulation in a realistic left heart," *Computers & Fluids*, vol. 94, pp. 173–187, May 2014. [Online]. Available: <https://doi.org/10.1016/j.compfluid.2014.01.030>
- [22] Y. Bazilevs, V. Calo *et al.*, "Variational multiscale residual-based turbulence modeling for large eddy simulation of incompressible flows," *Computer Methods in Applied Mechanics and Engineering*, vol. 197, no. 1–4, pp. 173–201, 2007.
- [23] J. Fuchsberger, P. Aigner *et al.*, "On the incorporation of obstacles in a fluid flow problem using a navier-stokes-brinkman penalization approach," 2021.
- [24] A. Daub, J. Kriegseis, and B. Frohnapfel, "Replication of left ventricular haemodynamics with a simple planar mitral valve model," *Biomedical Engineering / Biomedizinische Technik*, vol. 65, no. 5, pp. 595–603, 2020. [Online]. Available: <https://doi.org/10.1515/bmt-2019-0175>
- [25] Y. Zheng, A. Barbu *et al.*, "Four-chamber heart modeling and automatic segmentation for 3-d cardiac CT volumes using marginal space learning and steerable features," *IEEE Transactions on Medical Imaging*, vol. 27, no. 11, pp. 1668–1681, Nov. 2008. [Online]. Available: <https://doi.org/10.1109/tmi.2008.2004421>
- [26] M. Strocchi, C. M. Augustin *et al.*, "A publicly available virtual cohort of four-chamber heart meshes for cardiac electro-mechanics simulations," *PLOS ONE*, vol. 15, no. 6, p. e0235145, Jun. 2020. [Online]. Available: <https://doi.org/10.1371/journal.pone.0235145>
- [27] C. Rodero, M. Strocchi *et al.*, "Linking statistical shape models and simulated function in the healthy adult human heart," *PLOS Computational Biology*, vol. 17, no. 4, p. e1008851, Apr. 2021. [Online]. Available: <https://doi.org/10.1371/journal.pcbi.1008851>
- [28] A. Neic, M. A. Gsell *et al.*, "Automating image-based mesh generation and manipulation tasks in cardiac modeling workflows using meshtool," *SoftwareX*, vol. 11, p. 100454, Jan. 2020. [Online]. Available: <https://doi.org/10.1016/j.softx.2020.100454>
- [29] W. Shi, M. Jantsch *et al.*, "Temporal sparse free-form deformations," *Medical Image Analysis*, vol. 17, no. 7, pp. 779–789, Oct. 2013. [Online]. Available: <https://doi.org/10.1016/j.media.2013.04.010>
- [30] O. Razeghi, J. A. Solís-Lemus *et al.*, "CemrgApp: An interactive medical imaging application with image processing, computer vision, and machine learning toolkits for cardiovascular research," *SoftwareX*, vol. 12, p. 100570, Jul. 2020. [Online]. Available: <https://doi.org/10.1016/j.softx.2020.100570>
- [31] O. Razeghi, M. Strocchi *et al.*, "Tracking the motion of intracardiac structures aids the development of future leadless pacing systems," *Journal of Cardiovascular Electrophysiology*, vol. 31, no. 9, pp. 2431–2439, Jul. 2020. [Online]. Available: <https://doi.org/10.1111/jce.14657>
- [32] T. J. Hughes, W. K. Liu, and T. K. Zimmermann, "Lagrangian-eulerian finite element formulation for incompressible viscous flows," *Computer Methods in Applied Mechanics and Engineering*, vol. 29, no. 3, pp. 329–349, Dec. 1981. [Online]. Available: [https://doi.org/10.1016/0045-7825\(81\)90049-9](https://doi.org/10.1016/0045-7825(81)90049-9)
- [33] P. L. Tallec and J. Mouro, "Fluid structure interaction with large structural displacements," *Computer Methods in Applied Mechanics and Engineering*, vol. 190, no. 24–25, pp. 3039–3067, Mar. 2001. [Online]. Available: [https://doi.org/10.1016/s0045-7825\(00\)00381-9](https://doi.org/10.1016/s0045-7825(00)00381-9)
- [34] T. Engels, D. Kolomenskiy *et al.*, "FluSI: A novel parallel simulation tool for flapping insect flight using a fourier method with volume penalization," *SIAM Journal on Numerical Analysis*, vol. 38, no. 5, pp. S3–S24, Jan. 2016. [Online]. Available: <https://doi.org/10.1137/15m1026006>
- [35] P. Angot, C.-H. Bruneau, and P. Fabrie, "A penalization method to take into account obstacles in incompressible viscous flows," *Numerische Mathematik*, vol. 81, no. 4, pp. 497–520, Feb 1999.
- [36] K. E. Jansen, C. H. Whiting, and G. M. Hulbert, "A generalized- $\alpha$  method for integrating the filtered navier–stokes equations with a stabilized finite element method," *Computer Methods in Applied Mechanics and Engineering*, vol. 190, no. 3–4, pp. 305–319, Oct. 2000. [Online]. Available: [https://doi.org/10.1016/s0045-7825\(00\)00203-6](https://doi.org/10.1016/s0045-7825(00)00203-6)
- [37] R. S. Dembo, S. C. Eisenstat, and T. Steihaug, "Inexact newton methods," *SIAM Journal on Numerical Analysis*, vol. 19, no. 2, pp. 400–408, Apr. 1982. [Online]. Available: <https://doi.org/10.1137/0719025>
- [38] J. Fouchet-Incaux, "Artificial boundaries and formulations for the incompressible navier–stokes equations: applications to air and blood flows," *SeMA Journal*, vol. 64, no. 1, pp. 1–40, Jan. 2014. [Online]. Available: <https://doi.org/10.1007/s40324-014-0012-y>
- [39] E. Karabelas, M. A. F. Gsell *et al.*, "Towards a computational framework for modeling the impact of aortic coarctations upon left ventricular load," *Frontiers in Physiology*, vol. 9, May 2018. [Online]. Available: <https://doi.org/10.3389/fphys.2018.00538>
- [40] L. Marx, M. A. Gsell *et al.*, "Personalization of electro-mechanical models of the pressure-overloaded left ventricle: Fitting of Windkessel-type afterload models: Fitting of Windkessel afterload models," *Philos. Trans. R. Soc. A Math. Phys. Eng. Sci.*, vol. 378, no. 2173, 2020. [Online]. Available: <https://doi.org/10.1098/rsta.2019.0342>
- [41] G. Kovacs, A. Berghold *et al.*, "Pulmonary arterial pressure during rest and exercise in healthy subjects: a systematic review," *European Respiratory Journal*, vol. 34, no. 4, pp. 888–894, Mar. 2009. [Online]. Available: <https://doi.org/10.1183/09031936.00145608>
- [42] M. Braack and P. B. Mucha, "Directional do-nothing condition for the navier-stokes equations," *Journal of Computational Mathematics*, vol. 32, no. 5, pp. 507–521, Jun. 2014. [Online]. Available: <https://doi.org/10.4208/jcm.1405-m4347>
- [43] S. Longobardi, A. Lewalle *et al.*, "Predicting left ventricular contractile function via Gaussian process emulation in aortic-banded rats," *Philos Trans A Math Phys Eng Sci*, vol. 378, no. 2173, p. 20190334, Jun 2020.
- [44] A. O'Hagan, "Bayesian analysis of computer code outputs: A tutorial," *Reliability Engineering & System Safety*, vol. 91, no. 10, pp. 1290 – 1300, 2006, the Fourth International Conference on Sensitivity Analysis of Model Output (SAMO 2004). [Online]. Available: <https://doi.org/10.1016/j.ress.2005.11.025>
- [45] M. G. Genton, "Classes of kernels for machine learning: A statistics perspective," *J. Mach. Learn. Res.*, vol. 2, p. 299–312, Mar. 2002. [Online]. Available: <https://doi.org/10.5555/944790.944815>
- [46] E. Vigmond, R. W. dos Santos *et al.*, "Solvers for the cardiac bidomain equations," *Progress in Biophysics and Molecular Biology*, vol. 96, no. 1–3, pp. 3–18, Jan. 2008. [Online]. Available: <https://doi.org/10.1016/j.pbiomolbio.2007.07.012>
- [47] C. M. Augustin, A. Neic *et al.*, "Anatomically accurate high resolution modeling of human whole heart electromechanics: A strongly scalable algebraic multigrid solver method for nonlinear deformation," *Journal of Computational Physics*, vol. 305, pp. 622–646, Jan. 2016. [Online]. Available: <https://doi.org/10.1016/j.jcp.2015.10.045>
- [48] S. Kucherenko *et al.*, "Global sensitivity indices for nonlinear mathematical models, review," *Wilmott Mag*, vol. 1, pp. 56–61, 2005.
- [49] N. P. Johnson, J. M. Zelis *et al.*, "Pressure gradient vs. flow relationships to characterize the physiology of a severely stenotic aortic valve before and after transcatheter valve implantation," *European Heart Journal*, vol. 39, no. 28, pp. 2646–2655, Apr. 2018. [Online]. Available: <https://doi.org/10.1093/eurheartj/ehy126>
- [50] C. C. Long, M. Esmaily-Moghadam *et al.*, "Computation of residence time in the simulation of pulsatile ventricular assist devices," *Computational Mechanics*, vol. 54, no. 4, pp. 911–919, sep 2013. [Online]. Available: <https://doi.org/10.1007/s00466-013-0931-y>
- [51] V. John and E. Schmeyer, "Finite element methods for time-dependent convection–diffusion–reaction equations with small diffusion," *Computer Methods in Applied Mechanics and Engineering*, vol. 198, no. 3–4, pp. 475–494, Dec. 2008. [Online]. Available: <https://doi.org/10.1016/j.cma.2008.08.016>
- [52] A. Saltelli, P. Annoni *et al.*, "Variance based sensitivity analysis of model output. design and estimator for the total sensitivity index," *Computer Physics Communications*, vol. 181, no. 2, pp. 259–270, Feb. 2010. [Online]. Available: <https://doi.org/10.1016/j.cpc.2009.09.018>
- [53] J. Herman and W. Usher, "Salib: An open-source python library for sensitivity analysis," *Journal of Open Source Software*, vol. 2, no. 9, p. 97, 2017. [Online]. Available: <https://doi.org/10.21105/joss.00097>
- [54] B. E. Griffith, R. D. Hornung *et al.*, *Parallel and Adaptive Simulation of Cardiac Fluid Dynamics*. John Wiley & Sons, Ltd, 2009, ch. 7, pp. 105–130. [Online]. Available: <https://doi.org/10.1002/9780470558027.ch7>
- [55] D. Forti and L. Dedè, "Semi-implicit BDF time discretization of the navier–stokes equations with VMS-LES modeling in a high performance computing framework," *Computers & Fluids*, vol. 117, pp. 168–182, Aug. 2015. [Online]. Available: <https://doi.org/10.1016/j.compfluid.2015.05.011>
- [56] A. C. Daub, *Numerical Haemodynamics in the Human Heart*. Karlsruhe: KIT Scientific Publishing, Mar 2018. [Online]. Available: <https://doi.org/10.5445/KSP/1000080044>
- [57] L. Sun, H. Gao *et al.*, "Surrogate modeling for fluid flows based on physics-constrained deep learning without simulation data," *Computer Methods in Applied Mechanics and Engineering*, vol. 361, p. 112732, Apr. 2020. [Online]. Available: <https://doi.org/10.1016/j.cma.2019.112732>



# Supplementary Material for “Global Sensitivity Analysis of Four Chamber Heart Hemodynamics Using Surrogate Models”

E. Karabelas, S. Longobardi, J. Fuchsberger, O. Razeghi, C. Rodero,  
R. Rajani, M. Strocchi, G. Haase, G. Plank, and S. Niederer

November 18, 2021

## S.I. Residual-Based Variational Multiscale Formulation for Navier-Stokes-Brinkman Equations on moving domains

The Navier-Stokes-Brinkman (NSB) equations, originating from porous media theory, can be employed with the purpose of simulating viscous flow including complex shaped solid obstacles in a fluid domain, see [S2], and [S1, S11] for a in-depth mathematical analysis. The NSB model was successfully extended to moving obstacles and applied to model flapping insect flight in [S13]. In the present work, we use the NSB equations including the adaptation for moving obstacles as well as moving domains using the *arbitrary lagrangian Eulerian* (ALE) formulation [S20, S22, S40]:

$$\rho \left( \frac{\partial}{\partial t} \mathbf{u} + (\mathbf{u} - \mathbf{w}) \cdot \nabla \mathbf{u} \right) - \nabla \cdot \boldsymbol{\sigma}(\mathbf{u}, p) + \frac{\mu}{K} (\mathbf{u} - \mathbf{u}_s) = 0 \quad \text{in } \mathbb{R}^+ \times \Omega(t), \quad (1)$$

$$\nabla \cdot \mathbf{u} = 0 \quad \text{in } \mathbb{R}^+ \times \Omega(t), \quad (2)$$

$$\mathbf{u} = \mathbf{w} \quad \text{on } \Gamma_{\text{noslip}}(t), \quad (3)$$

$$\boldsymbol{\sigma} \mathbf{n} - \rho \beta ((\mathbf{u} - \mathbf{w}) \cdot \mathbf{n})_- = \mathbf{h} \quad \text{on } \Gamma_{\text{outflow}}(t), \quad (4)$$

$$\mathbf{u} = \mathbf{g} \quad \text{on } \Gamma_{\text{inflow}}(t), \quad (5)$$

$$\mathbf{u}|_{t=0} = \mathbf{u}_0, \quad (6)$$

with the time dependent fluid domain  $\Omega(t)$  defined as

$$\Omega(t) := \{ \mathbf{x} \mid \mathbf{x} = \mathbf{X} + \mathbf{d}(\mathbf{X}, t), \forall \mathbf{X} \in \Omega_0 \},$$

using the ALE mapping  $\mathbf{d}$  transforming an arbitrary reference configuration  $\Omega_0$  into the current fluid domain  $\Omega(t)$ . Here  $p$ ,  $\mathbf{u}$ , and  $\mathbf{w} := \frac{\partial}{\partial t} \mathbf{d}$  represent the fluid pressure, the flow velocity, and the ALE velocity respectively,  $\mu$  is the dynamic viscosity and  $\rho$  the density. The volume penalization term  $\frac{\mu}{K(t, \mathbf{x})} \mathbf{u}(t, \mathbf{x})$  is commonly known as *Darcy drag* which is characterized by the permeability  $K(t, \mathbf{x})$ . In (1) the Darcy drag is modified to enforce correct no-slip conditions

for obstacles moving with the obstacle velocity  $\mathbf{u}_s(\mathbf{x}, t)$ . The fluid stress tensor  $\boldsymbol{\sigma}(\mathbf{u}, p)$  and strain rate tensor  $\boldsymbol{\epsilon}(\mathbf{u}, p)$  are defined as follows:

$$\boldsymbol{\sigma}(\mathbf{u}, p) = -p\mathbf{I} + 2\mu\boldsymbol{\epsilon}(\mathbf{u}, p), \quad (7)$$

$$\boldsymbol{\epsilon}(\mathbf{u}, p) = \frac{1}{2}(\nabla\mathbf{u} + (\nabla\mathbf{u})^\top). \quad (8)$$

For  $\mathbf{h} = \mathbf{0}$ , (4) is known as a directional do-nothing boundary condition [S9, S33], where  $\mathbf{n}$  is the outward normal of the fluid domain,  $\beta \leq \frac{1}{2}$  is a positive constant and (9) is added for backflow stabilization with

$$((\mathbf{u} - \mathbf{w}) \cdot \mathbf{n})_- := \frac{1}{2}((\mathbf{u} - \mathbf{w}) \cdot \mathbf{n} - |(\mathbf{u} - \mathbf{w}) \cdot \mathbf{n}|). \quad (9)$$

The ALE domain  $\Omega(t)$  is split up into three time dependent sub-domains by means of the permeability  $K(t, \mathbf{x})$ , namely the fluid sub-domain  $\Omega_f(t)$ , the porous sub-domain  $\Omega_p(t)$  and the solid sub-domain  $\Omega_s(t)$ .

$$K(t, \mathbf{x}) = \begin{cases} K_f \rightarrow +\infty & \text{if } \mathbf{x} \in \Omega_f(t) \\ K_p & \text{if } \mathbf{x} \in \Omega_p(t) \\ K_s \rightarrow 0^+ & \text{if } \mathbf{x} \in \Omega_s(t) \end{cases} \quad (10)$$

In  $\Omega_f(t)$  the classical ALE-Navier–Stokes equations are recovered, while in  $\Omega_p$  the full ALE-NSB equations describe fluid flowing through a moving porous medium,  $\mathbf{u}$  and  $p$  are understood in an averaged sense in this context. In  $\Omega_s(t)$  the velocity  $\mathbf{u}$  is approaching  $\mathbf{u}_s$  and thus asymptotically satisfying the no-slip condition on the  $\Omega_f(t)/\Omega_s(t)$  interface. Note that even in the case where  $K \rightarrow 0^+$  the penalization term has a well defined limit, see [S1].

### S.1.A. Hemodynamic Afterload Models

Modeling of afterload for hemodynamics is modeled by using a 0D Windkessel model. This means we define  $\mathbf{h}$  in (4) as

$$\mathbf{h} := -p_{\text{WK}}(t)\mathbf{n}$$

with the *Windkessel pressure*  $p_{\text{WK}}$  is governed by the differential algebraic system [S16]

$$C_{\text{WK}} \frac{d}{dt} p_d(t) + \frac{p_d(t)}{R_{\text{WK}}} = Q(t), \quad (11)$$

$$p_{\text{WK}}(t) = Z_{\text{WK}} Q(t) + p_d(t), \quad (12)$$

$$Q(t) := \int_{\Gamma_{\text{outflow}}} \mathbf{u} \cdot \mathbf{n} \, ds_{\mathbf{x}}. \quad (13)$$

In the case of multiple Windkessel outlets we will use the same notation for variables with an added  $i$  subscript indicating multiple outlets. Tools for personalization of the individual Windkessel parameters can be found in [S32].

### S.I.B. Variational Formulation and Numerical Stabilization

Following [S7, S8] the discrete variational formulation of (1) including the boundary conditions (4), (5) and (3) can be stated in the following abstract form: Find  $\mathbf{u}^h \in [\mathcal{S}_{h,g}^1(\mathcal{T}_N)]^3$ ,  $p^h \in \mathcal{S}_h^1(\mathcal{T}_N)$  such that, for all  $\mathbf{v}^h \in [\mathcal{S}_{h,0}^1(\mathcal{T}_N)]^3$  and for all  $q^h \in \mathcal{S}_h^1(\mathcal{T}_N)$

$$A_{\text{NS}}(\mathbf{v}^h, q^h; \mathbf{u}^h, p^h) + S_{\text{RBVMS}}(\mathbf{v}^h, q^h; \mathbf{u}^h, p^h) = F_{\text{NS}}(\mathbf{v}^h) \quad (14)$$

with the bilinear form of the NSB equations

$$\begin{aligned} A_{\text{NS}}(\mathbf{v}^h, q^h; \mathbf{u}^h, p^h) = & \int_{\Omega} \rho \mathbf{v}^h \cdot \left[ \left( \frac{\partial \mathbf{u}^h}{\partial t} + (\mathbf{u}^h - \mathbf{w}) \cdot \nabla \mathbf{u}^h + \frac{\nu}{K} (\mathbf{u}^h - \mathbf{u}_s^h) \right) + \varepsilon(\mathbf{v}^h) : \boldsymbol{\sigma}(\mathbf{u}^h, p^h) \right] dx \\ & - \int_{\Gamma_{\text{outflow}}} \rho \beta ((\mathbf{u}^h - \mathbf{w}) \cdot \mathbf{n})_- \mathbf{v}^h \cdot \mathbf{u}^h ds_x + \int_{\Omega} q^h \nabla \cdot \mathbf{u}^h dx, \end{aligned} \quad (15)$$

the bilinear form  $S_{\text{RBVMS}}$ , which will be explained later in Equation (21), and the right hand side contribution

$$F_{\text{NS}} = -p_{\text{WK}} \int_{\Gamma_{\text{outflow}}} \mathbf{n} \cdot \mathbf{v}_h ds_x. \quad (16)$$

We use standard notation to describe the finite element function space  $\mathcal{S}_{h,*}^1(\mathcal{T}_N)$  as a conformal trial space of piece-wise linear, globally continuous basis functions  $v_h$  over a decomposition  $\mathcal{T}_N$  of  $\Omega$  into  $N$  finite elements constrained by  $v_h = *$  on essential boundaries. The space  $\mathcal{S}_h^1(\mathcal{T}_N)$  denotes the same space without constraints. For further details we refer to [S10, S39]. As previously described in [S26] we utilize the residual based variational multiscale (RBVMS) formulation as proposed in [S7, S8], providing turbulence modeling in addition to numerical stabilization. In the following we give a short summary of the changes necessary to use RBVMS methods for the ALE-NSB equations. Briefly, the RBVMS formulation is based on a decomposition of the solution and weighting function spaces into coarse and fine scale subspaces and the corresponding decomposition of the velocity and the pressure and their respective test functions. Henceforth the fine scale quantities and their respective test functions shall be denoted with the superscript  $'$ . We assume  $\mathbf{u}_s = \mathbf{u}_s^h$ , quasi-static fine scales ( $\frac{\partial \mathbf{u}'}{\partial t} = 0$ ), as well as  $\frac{\partial \mathbf{u}^h}{\partial t} = 0$ ,  $\mathbf{u}' = \mathbf{0}$  on  $\partial\Omega(t)$  and incompressibility conditions for  $\mathbf{u}^h$  and  $\mathbf{u}'$ . The fine scale pressure and velocity are approximated in an element-wise manner by means of the residuals  $\mathbf{r}_M$  and  $r_C$ .

$$\mathbf{u}' = -\frac{\tau_{\text{SUPS}}}{\rho} \mathbf{r}_M(\mathbf{u}^h, p^h) \quad (17)$$

$$p' = -\rho \nu_{\text{LSIC}} r_C(\mathbf{u}^h) \quad (18)$$

The residuals of the NSB equations and the incompressibility constraint are:

$$\mathbf{r}_M(\mathbf{u}^h, p^h) = \rho \frac{\partial}{\partial t} \mathbf{u}^h + \rho (\mathbf{u}^h - \mathbf{w}) \cdot \nabla \mathbf{u}^h - \nabla \cdot \boldsymbol{\sigma}(\mathbf{u}^h, p^h) + \frac{\mu}{K} (\mathbf{u}^h - \mathbf{u}_s^h) \quad (19)$$

$$r_C(\mathbf{u}^h) = \nabla \cdot \mathbf{u}^h \quad (20)$$

Taking all assumptions into consideration and employing the scale decomposition followed by partial integration yields the bilinear form of the RBVMS formulation  $S_{\text{RBVMS}}(\mathbf{v}^h, q^h; \mathbf{u}^h, p^h)$ ,

$$\begin{aligned}
S_{\text{RBVMS}}(\mathbf{v}^h, q^h; \mathbf{u}^h, p^h) = & \\
& + \sum_{\Omega_e \in \mathcal{T}_N} \int_{\Omega_e} \tau_{\text{SUPS}} \left( (\mathbf{u}^h - \mathbf{w}) \cdot \nabla \mathbf{v}^h + \frac{1}{\rho} \nabla q^h - \frac{\nu}{K} \mathbf{v}^h \right) \mathbf{r}_M(\mathbf{u}^h, p^h) \, d\mathbf{x} \\
& + \sum_{\Omega_e \in \mathcal{T}_N} \int_{\Omega_e} \rho \nu_{\text{LSIC}} \nabla \cdot \mathbf{v}^h r_C(\mathbf{u}^h) \, d\mathbf{x} \\
& - \sum_{\Omega_e \in \mathcal{T}_N} \int_{\Omega_e} \tau_{\text{SUPS}} \mathbf{v}^h \cdot \left( \mathbf{r}_M(\mathbf{u}^h, p^h) \cdot \nabla \mathbf{u}^h \right) \, d\mathbf{x} \\
& - \sum_{\Omega_e \in \mathcal{T}_N} \int_{\Omega_e} \frac{\tau_{\text{SUPS}}^2}{\rho} \nabla \mathbf{v}^h : \left( \mathbf{r}_M(\mathbf{u}^h, p^h) \otimes \mathbf{r}_M(\mathbf{u}^h, p^h) \right) \, d\mathbf{x}.
\end{aligned} \tag{21}$$

The residuals (19) and (20) are evaluated for every element  $\Omega_e \in \mathcal{T}_N$ . Following [S36] the stabilization parameters  $\tau_{\text{SUPS}}$  and  $\nu_{\text{LSIC}}$  are defined as:

$$\tau_{\text{SUPS}} := \left( \frac{4}{\Delta t^2} + (\mathbf{u}^h - \mathbf{w}) \cdot \mathbf{G}(\mathbf{u}^h - \mathbf{w}) + \left( \frac{\nu}{K} \right)^2 + C_I \nu^2 \mathbf{G} : \mathbf{G} \right)^{-\frac{1}{2}} \tag{22}$$

$$\nu_{\text{LSIC}} := \frac{1}{\text{tr}(\mathbf{G}) \tau_{\text{SUPS}}} \tag{23}$$

Here  $\mathbf{G}$  is the three dimensional element metric tensor defined per finite element as

$$\mathbf{G}|_{\tau_l} := \mathbf{J}_l^{-1} \mathbf{J}_l^{-\top},$$

with  $\mathbf{J}_l$  being the Jacobian of the transformation of the reference element to the physical finite element  $\tau_l \in \mathcal{T}_N$ ,  $\Delta t$  denotes time step size and  $C_I$  is a positive constant, taken as 30, derived from an element-wise inverse estimate. For further details see [S7, S8].

### S.I.C. Numerical Solution Strategy

Spatio-temporal discretization of all PDEs and the solution of the arising systems of equations relied upon the Cardiac Arrhythmia Research Package (CARPentry), see [S42]. For temporal discretization of the ALE-NSB equations we used the generalized- $\alpha$  method, see [S23] with a spectral radius  $\rho_\infty = 0.2$ . For updating the Windkessel pressures  $p_{\text{WK}}$  we discretized (11) with an implicit Euler method. For ease of coupling with our CFD solver the calculation of  $Q(t)$  in (13) is lagged by one Newton iteration. After discretization in space as described in Section S.I.B and temporal discretization using the generalized- $\alpha$  integrator we obtain a nonlinear algebraic system to solve for advancing time from timestep  $t_n$  to  $t_{n+1}$ . A quasi inexact Newton-Raphson method is used to solve this system with linearization approach similar to [S8] adapted to the NSB equations. At each iteration a block system of the form

$$\begin{bmatrix} \mathbf{K}_h & \mathbf{B}_h \\ \mathbf{C}_h & \mathbf{D}_h \end{bmatrix} \begin{bmatrix} \Delta \mathbf{u} \\ \Delta \mathbf{p} \end{bmatrix} = - \begin{bmatrix} -\mathbf{R}_{\text{upper}} \\ -\mathbf{R}_{\text{lower}} \end{bmatrix},$$

is solved with  $\mathbf{K}_h$ ,  $\mathbf{B}_h$ ,  $\mathbf{C}_h$ , and  $\mathbf{D}_h$  denoting the Jacobian matrices,  $\Delta \mathbf{u}$ ,  $\Delta \mathbf{p}$  representing the velocity and pressure updates and  $\mathbf{R}_{\text{upper}}$ ,  $\mathbf{R}_{\text{lower}}$  indicating the residual contributions. In

this regard we use the flexible generalized minimal residual method (fGMRES) and efficient preconditioning based on the PCFIELDSPLIT<sup>1</sup> package from the library *PETSc* [S4-S6] and the incorporated suite *HYPRE BoomerAMG* [S19]. By extending our previous work [S3, S26, S27] we implemented the methods in the finite element code *Cardiac Arrhythmia Research Package* (CARPentry) [S41, S42].

## S.II. Obstacle Representation

Here we want to give a brief description of how we represent moving obstacles for usage in the ALE-NSB equations. This task is solved by representing obstacles using triangular surface meshes followed by element-wise calculation of the partial volume covered by the obstacle. In the first step, all nodes within the obstacle are identified using the ray casting algorithm [S18, S34]. Subsequently, all elements are split into three categories and receive a corresponding volume fraction value  $v_f$ , describing the partial volume covered by the obstacle:

- Elements fully covered by the obstacle lie in  $\Omega_s$ , consequently  $v_f = 1$ .
- Elements outside the obstacle lie in  $\Omega_f$  and obtain  $v_f = 0$ .
- Elements that are split by the element surface correspond to elements in  $\Omega_p$ , hence

$$v_f = \frac{V_{in}}{V_{tot}} \quad (24)$$

where  $V_{in}$  denotes the element volume covered by the obstacle and  $V_{tot}$  is the total element volume.

This procedure is carried out for every time step and yields a time-dependent, element-based volume fraction distribution  $v_f(t, \mathbf{x})$ , that serves as a basis to provide a suitable permeability distribution, see Figure S1. In this work we define  $\frac{1}{K(t, \mathbf{x})} := \frac{v_f(t, \mathbf{x})}{\kappa}$  with  $\kappa$  being a fixed penalization factor, e.g.  $\kappa = 10^{-8}$ . All permeability distributions in this work have been generated using the open-source software *Meshtool*<sup>2</sup>, see [S35] and [S17] for algorithmic details. In the case of obstacles that change from open to closed state over time we use a simple scaling function. For example, assume an obstacle representing a heart valve region will be open at a time instance  $t_{op}$  and it takes  $\text{dur}_V$  time to switch from open to closed we define

$$\chi(t) := \begin{cases} \frac{t_{op}-t}{\text{dur}_V} & t \in [t_{op} - \text{dur}_V, t_{op}] \\ 0 & t \in [t_{op}, t_{cl} - \text{dur}_V] \\ \frac{t-t_{cl}+\text{dur}_V}{\text{dur}_V} & t \in [t_{cl} - \text{dur}_V, t_{cl}] \\ 1 & \text{else} \end{cases}, \quad (25)$$

and modify  $\frac{1}{K(t, \mathbf{x})}$  to  $\frac{\chi}{K(t, \mathbf{x})}$ .

<sup>1</sup><https://www.mcs.anl.gov/petsc/petsc-current/docs/manualpages/PC/PCFIELDSPLIT.html>

<sup>2</sup><https://bitbucket.org/aneic/meshtool/src/master/>

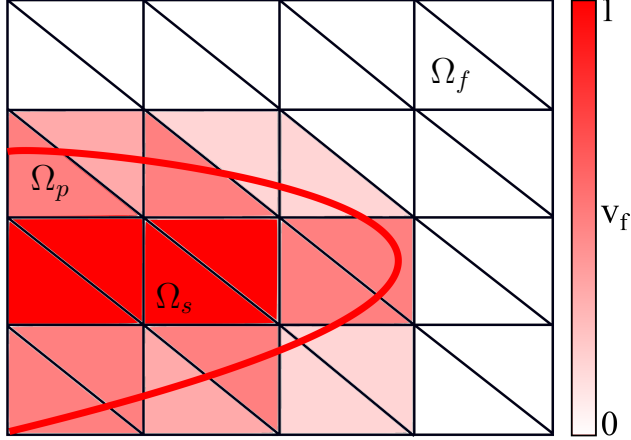


Figure S1.: Schematic representation of the  $v_f$  distribution associated to an obstacle, which is represented by the red line, at fixed time  $t$ .

### S.III. Computation of Residence Times on Moving Domains

Here we will give a brief outline of the methods and algorithms used to compute residence time distributions. The starting point is the following PDE describing the time evolution of a residence time distribution field originating from [S14, S30]. Given a moving fluid domain  $\Omega(t) \subset \mathbb{R}^3$  and a region of interest  $V(t) \subset \Omega(t)$  the evolution of the time  $\tau(t, \mathbf{x})$  spent in  $V$  by an arbitrarily small fluid particle caught at point  $\mathbf{x} \in \Omega(t)$  at time  $t$  can be described as

$$\begin{aligned}
 \frac{\partial}{\partial t} \tau + (\mathbf{u} - \mathbf{w}) \cdot \nabla \tau - \varepsilon \Delta \tau &= H(t, \mathbf{x}) && \text{in } \Omega(t), \\
 \frac{\partial}{\partial \mathbf{n}} \tau &= 0 && \text{on } \Gamma_N(t), \\
 \tau &= g && \text{on } \Gamma_D(t), \\
 H(t, \mathbf{x}) &:= \begin{cases} 1 & \text{if } (t, \mathbf{x}) \in V(t) \\ 0 & \text{else} \end{cases},
 \end{aligned}$$

with the fluid velocity  $\mathbf{u}$ , the ALE mesh velocity  $\mathbf{w}$  and a small artificial diffusion parameter  $\varepsilon$ . Throughout this work we have used  $\varepsilon = 1 \times 10^{-12}$ . The fluid velocity  $\mathbf{u}$  as well as the ALE mesh velocity  $\mathbf{w}$  are assumed to be given functions, e.g. coming from a pre-computed CFD simulation. In our applications we set  $\Gamma_D(t) = \emptyset$  and  $\Gamma_N(t) = \partial\Omega(t)$ . Furthermore, the region of interest  $V(t)$  is assumed as a time-evolving tag region assigned to a particular anatomic region, e.g.: ventricular blood pools, and left atrial appendage respectively. After discretization we have

$$\mathbf{M}_h(t) \dot{\boldsymbol{\tau}} + \mathbf{K}_h(t) \boldsymbol{\tau}(t) = \mathbf{F}_h(t) \tag{26}$$

with

$$\begin{aligned}
\mathbf{M}_{h,ij}(t) &= \int_{\Omega(t)} \phi_i(t)\phi_j(t) \, dx, \\
\mathbf{K}_{h,ij}(t) &= \varepsilon \int_{\Omega(t)} \nabla\phi_i(t) \cdot \nabla\phi_j(t) \, dx \\
&\quad + \int_{\Omega(t)} (\mathbf{u}(t) - \mathbf{w}(t)) \cdot \nabla\phi_i(t)\phi_j(t) \, dx, \\
\mathbf{F}_{h,j}(t) &= \int_{\Omega(t)} f(t)\phi_j(t) \, dx,
\end{aligned}$$

with  $\{\phi_i(t)\}_{i=0}^n$  being the time-dependent test and trials functions in the ALE domain. For regular domain movement it is safe to assume that  $\mathbf{M}_h(t)$  is invertible for all  $t$  and we can rewrite (26) as

$$\dot{\boldsymbol{\tau}} + \mathbf{M}_h^{-1}(t)\mathbf{K}_h(t)\boldsymbol{\tau}(t) = \mathbf{M}_h^{-1}(t)\mathbf{F}_h(t). \quad (27)$$

Next, we apply the modified Crank-Nicholson scheme in time as proposed in [S15] giving

$$\left(\mathbf{M}_C + \frac{\Delta t}{2}\mathbf{K}\right)\boldsymbol{\tau}^{n+1} = \left(\mathbf{M}_C - \frac{\Delta t}{2}\mathbf{K}\right)\boldsymbol{\tau}^n + \frac{\Delta t}{2}\mathbf{F}, \quad (28)$$

where we used the following shorthand notation

$$\begin{aligned}
\mathbf{M}_C &:= \mathbf{M}_h(t^{n+\frac{1}{2}}), \\
\mathbf{K} &:= \mathbf{K}_h(t^{n+\frac{1}{2}}), \\
\mathbf{F} &:= \mathbf{F}_h(t^{n+\frac{1}{2}}).
\end{aligned}$$

Equation (28) is our starting point for applying the FCT scheme similar to [S25]. Following the ideas of FEM-FCT methods we define the matrices

$$\begin{aligned}
\mathbf{L} &:= \mathbf{K} + \mathbf{D}, \\
\mathbf{D}_{ij} &= -\max\{0, \mathbf{K}_{ij}, \mathbf{K}_{ji}\} && \text{if } i \neq j, \\
\mathbf{D}_{ii} &= -\sum_{j=1, j \neq i}^N \mathbf{D}_{ij} && \text{else,} \\
\mathbf{M}_L &= \text{diag}(\mathbf{m}), \\
\mathbf{m}_i &= \sum_{j=1}^N \mathbf{M}_{C,ij}.
\end{aligned}$$

The construction of  $\mathbf{L}$  ensures zero row and column sums. Instead of (28) we consider

$$\left(\mathbf{M}_L + \frac{\Delta t}{2}\mathbf{L}\right)\boldsymbol{\tau}^{n+1} = \left(\mathbf{M}_L - \frac{\Delta t}{2}\mathbf{L}\right)\boldsymbol{\tau}^n + \frac{\Delta t}{2}\mathbf{F}, \quad (29)$$

which represents a stable low-order scheme whose solution doesn't possess any over or under-shoots but suffers from smeared layers. To correct this behavior and artificial flux correction

vector  $\mathbf{f}^*(\tau^{n+1}, \tau^n)$  is added to the right hand side of (29). The definition of  $\mathbf{f}^*$  follows from an ad-hoc ansatz

$$\mathbf{f}_i^*(\tau^{n+1}, \tau^n) = \sum_{j=1}^n \alpha_{ij} r_{ij},$$

with the *fluxes*  $r_{ij}$  defined as

$$\begin{aligned} r_{ij} := & \mathbf{M}_{C,ij}(\tau_i^{n+1} - \tau_j^{n+1}) - \mathbf{M}_{C,ij}(\tau_i^n - \tau_j^n) \\ & - \frac{\Delta t}{2} \mathbf{D}_{ij}(\tau_i^{n+1} - \tau_j^{n+1}) - \frac{\Delta t}{2} \mathbf{D}_{ij}(\tau_i^n - \tau_j^n). \end{aligned} \quad (30)$$

and weights  $\alpha_{ij} \in [0, 1]$ . The representation for  $r_{ij}$  follows from first subtracting (28) from (29) and applying the properties of the matrices  $\mathbf{M}_C$  and  $\mathbf{D}$ . This formulation represents a nonlinear system. In [S25] a linear variant has been proposed which we adapted to the moving-domain case. For this we use the explicit solution  $\tilde{\tau}$  to (29), by means of an explicit Euler scheme approximating the solution  $\tau^{n+\frac{1}{2}}$  at time step  $t_n + \frac{\Delta t}{2}$ , reading

$$\tilde{\tau} := \tau^n - \frac{\Delta t}{2} \mathbf{M}_L^{-1} (\mathbf{L}\tau^n - \mathbf{F}).$$

Inserting  $\tilde{\tau}$  into (30) and rearranging terms yields

$$r_{ij} = \Delta t \left( \mathbf{M}_{C,ij}(\boldsymbol{\eta}_i^{n+\frac{1}{2}} - \boldsymbol{\eta}_j^{n+\frac{1}{2}}) - \mathbf{D}_{ij}(\tilde{\tau}_i - \tilde{\tau}_j) \right),$$

where  $\boldsymbol{\eta}_i^{n+\frac{1}{2}} := (\mathbf{M}_L^{-1}(\mathbf{F} - \mathbf{L}\tau^n))_i$ . Additionally, as suggested in [S28], we employ prelimiting in the form

$$r_{ij} = 0 \quad \text{if } r_{ij}(\tilde{\tau}_i - \tilde{\tau}_j) < 0.$$

The computation of the weights  $\alpha_{ij}$  follows the same procedure as in [S25] using Zalesak's algorithm [S43]. We also refer to [S28, S29] for a more detailed overview of the presented method. Computation of the residence time distribution fields have been included as add-on in *CARPentry*. After computation of the residence time distribution  $\tau$  we can calculate the residence time RT spend in  $V(t)$  over a time period  $(t_0, t_1)$  [S30] as

$$\begin{aligned} \text{RT} &:= \frac{1}{(t_1 - t_0)|V|} \int_{t_0}^{t_1} \int_{\Omega(t)} \tau(t, \mathbf{x}) H(t, \mathbf{x}) \, d\mathbf{x} dt, \\ |V| &:= \frac{1}{t_1 - t_0} \int_{t_0}^{t_1} \int_{\Omega(t)} H(t, \mathbf{x}) \, d\mathbf{x} dt. \end{aligned}$$

Figure S2 and Figure S3 show illustrations of time averaged residence time distributions that were generated for this work as part of the sensitivity analysis.

## S.IV. Pope's Criterion of Turbulence Resolution

In LES type formulations the resolved velocity field is fundamentally linked to the numerical method used, hence there is no notion of convergence to the solution of a partial differential



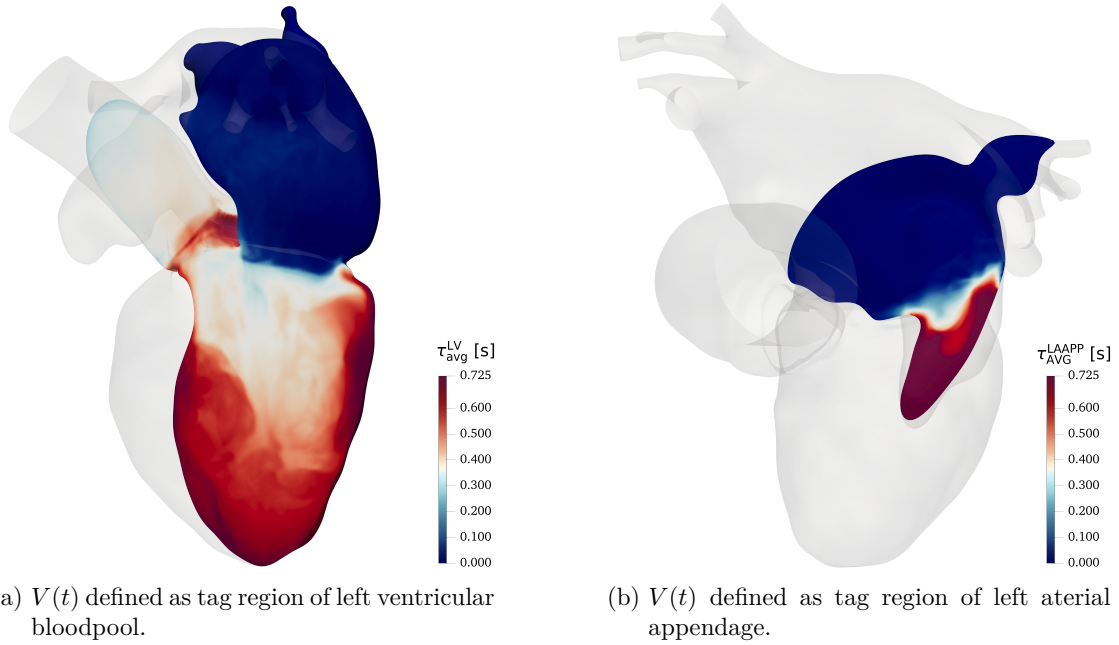


Figure S2.: Time-averaged residence time distributions  $\tau_{\text{AVG}}$  with  $V(t)$  defined through different labels in the computational mesh. Time average taken over the final two heartbeats with beatlength equal to 0.725 s.

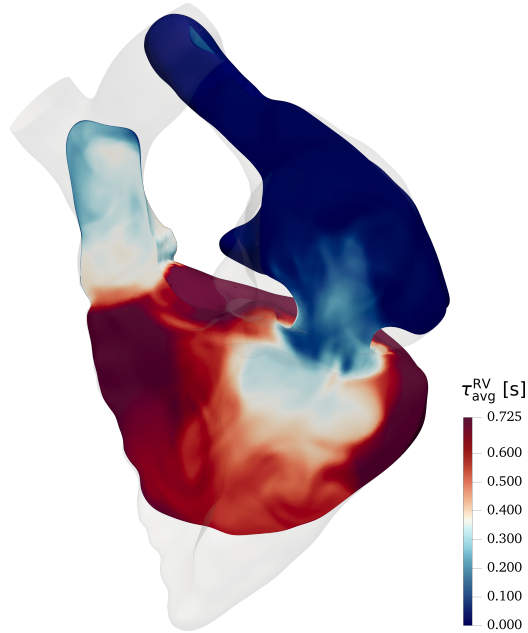


Figure S3.: Time-averaged residence time distributions  $\tau_{\text{AVG}}^{\text{RV}}$  with  $V(t)$  defined as right ventricular blood pool in the computational mesh. Time average taken over the final two heartbeats with beatlength equal to 0.725 s.

equation [S37]. This leads to the problem that mesh convergence often cannot be established by the classical methods [S12, S21, S24, S31, S38]. To remedy this problem [S37] proposes the use of a measure of turbulence resolution  $M$ , see (32), utilizing the fraction of turbulent kinetic energy resolved by the grid in question. In order to obtain a point-wise measure, rather than the kinetic energy itself, the kinetic energy density  $K(\mathbf{x}, t)$  is considered:

$$K(\mathbf{x}, t) = \frac{\rho}{2} \mathbf{u}(\mathbf{x}, t)^2. \quad (31)$$

The resulting point-wise measure of turbulence resolution  $M$  reads:

$$M(\mathbf{x}, t) = \frac{K'(\mathbf{x}, t)}{K_{tot}(\mathbf{x}, t)}. \quad (32)$$

Here  $K'$  is the turbulent kinetic energy of the residual motions, hence of the motions not resolved by the grid, and  $K_{tot}$  stands for the total kinetic energy.  $K_{tot}$  may be written as the sum of the resolved turbulent kinetic energy  $K^h$  and the not resolved turbulent kinetic energy  $K'$ :

$$K_{tot}(\mathbf{x}, t) = K^h(\mathbf{x}, t) + K'(\mathbf{x}, t) \quad (33)$$

The resolved turbulent kinetic energy  $K^h$  is calculated from (31) using the fluctuating part of the resolved fluid velocity  $\mathbf{u}_f$ , which is given by:

$$\mathbf{u}_f(\mathbf{x}, t) = \overline{\mathbf{u}^h}(\mathbf{x}, t) - \mathbf{u}^h(\mathbf{x}, t), \quad (34)$$

where  $\overline{\mathbf{u}^h}$  is an average with respect to time. When considering a constant inflow  $\overline{\mathbf{u}^h}$  is given by the standard mean over all time steps ( $t = 1 \dots T$ , hence  $\overline{\mathbf{u}^h}$  is not time-dependent) :

$$\overline{\mathbf{u}^h}(\mathbf{x}) = \frac{1}{T} \sum_{t=1}^T \mathbf{u}^h(\mathbf{x}, t) \quad (35)$$

In the case of a pulsatile behavior however a phase average is considered:

$$\overline{\mathbf{u}^h}(\mathbf{x}, t) = \frac{1}{n} \sum_{k=0}^{n-1} \mathbf{u}^h(\mathbf{x}, t + k\tau), \quad (36)$$

where  $n$  is the number of cycles or beats and  $\tau$  is the period or beat length. By the use of (32) a criterion for sufficient mesh resolution is given:

$$M(\mathbf{x}, t) \leq \epsilon_M \quad (37)$$

In [S37] a value of  $\epsilon_M = 0.2$  is proposed, which corresponds to requiring a minimum of 80% of the total turbulence energy to be resolved.

## S.V. Input Parameter Variance Effect on Output Features

This serves as additional interpretation for the results in the main manuscript. Figure S4 shows the extracted temporal signals of all parameter sets for the pressure differences  $\Delta p_{MV1,2,3,4}$  in the LA. While there is no strong influence on the output in systole, one can see a clear variation in the outputs in diastole.

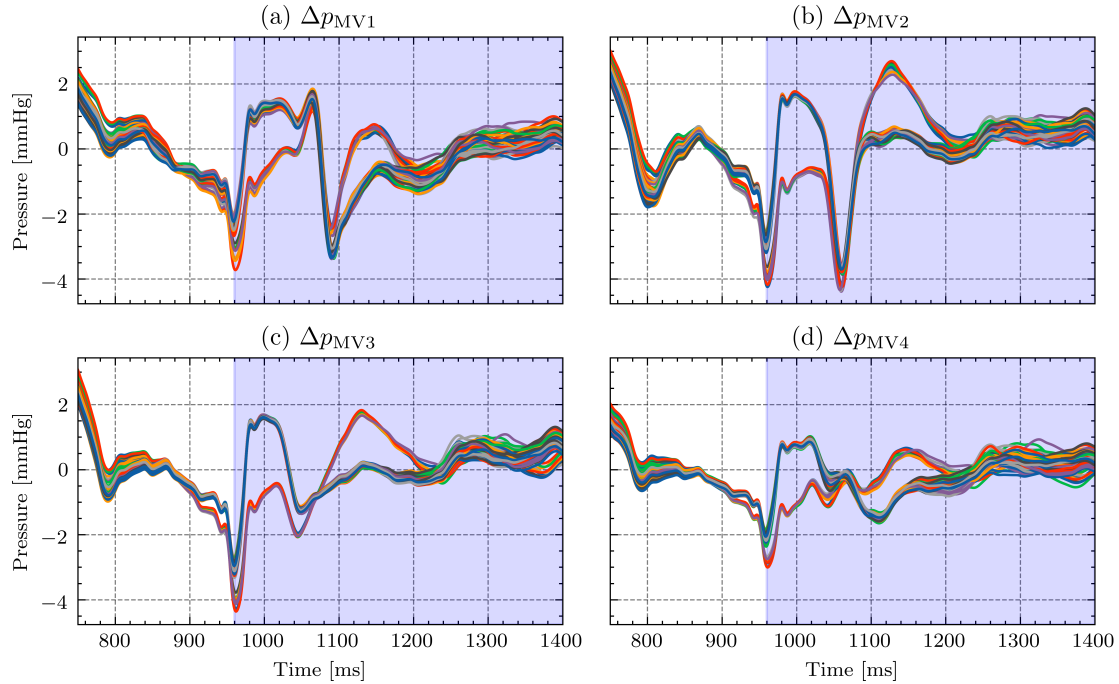


Figure S4.: Extracted time signals for pressure differences in the LA for the second heart beat. Diastole is indicated by the shaded blue area in the plots.

## References

- [S1] P. Angot, C.-H. Bruneau, and P. Fabrie. A penalization method to take into account obstacles in incompressible viscous flows. *Numerische Mathematik*, 81(4):497–520, Feb 1999. ISSN 0945-3245. doi: 10.1007/s002110050401.
- [S2] E. Arquis and J. Caltagirone. Sur les conditions hydrodynamiques au voisinage d’une interface milieu fluide-milieu poreux: application a la convection naturelle. *CR Acad. Sci. Paris II*, 299:1–4, 1984.
- [S3] C. M. Augustin, A. Neic, M. Liebmann, A. J. Prassl, S. A. Niederer, G. Haase, and G. Plank. Anatomically accurate high resolution modeling of human whole heart electromechanics: A strongly scalable algebraic multigrid solver method for nonlinear deformation. *Journal of Computational Physics*, 305:622–646, Jan. 2016. URL <https://doi.org/10.1016/j.jcp.2015.10.045>.
- [S4] S. Balay, W. D. Gropp, L. C. McInnes, and B. F. Smith. Efficient management of parallelism in object oriented numerical software libraries. In E. Arge, A. M. Bruaset, and H. P. Langtangen, editors, *Modern Software Tools in Scientific Computing*, pages 163–202. Birkhäuser Press, 1997.
- [S5] S. Balay, S. Abhyankar, M. F. Adams, J. Brown, P. Brune, K. Buschelman, L. Dalcin, A. Dener, V. Eijkhout, W. D. Gropp, D. Karpeyev, D. Kaushik, M. G. Knepley, D. A. May, L. C. McInnes, R. T. Mills, T. Munson, K. Rupp, P. Sanan, B. F. Smith, S. Zampini,

- H. Zhang, and H. Zhang. PETSc Web page. <https://www.mcs.anl.gov/petsc>, 2019. URL <https://www.mcs.anl.gov/petsc>.
- [S6] S. Balay, S. Abhyankar, M. F. Adams, J. Brown, P. Brune, K. Buschelman, L. Dalcin, A. Dener, V. Eijkhout, W. D. Gropp, D. Karpeyev, D. Kaushik, M. G. Knepley, D. A. May, L. C. McInnes, R. T. Mills, T. Munson, K. Rupp, P. Sanan, B. F. Smith, S. Zampini, H. Zhang, and H. Zhang. PETSc users manual. Technical Report ANL-95/11 - Revision 3.13, Argonne National Laboratory, 2020. URL <https://www.mcs.anl.gov/petsc>.
- [S7] Y. Bazilevs, V. Calo, J. Cottrell, T. Hughes, A. Reali, and G. Scovazzi. Variational multiscale residual-based turbulence modeling for large eddy simulation of incompressible flows. *Computer Methods in Applied Mechanics and Engineering*, 197(1-4):173–201, 2007. doi: 10.1016/j.cma.2007.07.016.
- [S8] Y. Bazilevs, K. Takizawa, and T. Tezduyar. *Computational Fluid-Structure Interaction: Methods and Applications*. John Wiley and Sons, 2013. ISBN 9780470978771. doi: 10.1002/9781118483565.
- [S9] M. Braack and P. B. Mucha. Directional do-nothing condition for the navier-stokes equations. *Journal of Computational Mathematics*, 32(5):507–521, June 2014. URL <https://doi.org/10.4208/jcm.1405-m4347>.
- [S10] S. Brenner and R. Scott. *The mathematical theory of finite element methods*, volume 15. Springer Science & Business Media, 2007.
- [S11] G. Carbou and P. Fabrie. Boundary layer for a penalization method for viscous incompressible flow. *Adv. Differential Equations*, 8(12):1453–1480, 2003.
- [S12] C. Chnafa, S. Mendez, and F. Nicoud. Image-based large-eddy simulation in a realistic left heart. *Computers & Fluids*, 94:173–187, May 2014. URL <https://doi.org/10.1016/j.compfluid.2014.01.030>.
- [S13] T. Engels, D. Kolomenskiy, K. Schneider, and J. Sesterhenn. FluSI: A novel parallel simulation tool for flapping insect flight using a fourier method with volume penalization. *SIAM Journal on Scientific Computing*, 38(5):S3–S24, Jan. 2016. URL <https://doi.org/10.1137/15m1026006>.
- [S14] M. Esmaily-Moghadam, T.-Y. Hsia, and A. L. Marsden. A non-discrete method for computation of residence time in fluid mechanics simulations. *Physics of Fluids*, 25(11): 110802, nov 2013. URL <https://doi.org/10.1063/1.4819142>.
- [S15] L. Formaggia and F. Nobile. Stability analysis of second-order time accurate schemes for ALE–FEM. *Computer Methods in Applied Mechanics and Engineering*, 193(39-41): 4097–4116, Oct. 2004. URL <https://doi.org/10.1016/j.cma.2003.09.028>.
- [S16] J. Fouchet-Incaux. Artificial boundaries and formulations for the incompressible navier–stokes equations: applications to air and blood flows. *SeMA Journal*, 64(1): 1–40, Jan. 2014. URL <https://doi.org/10.1007/s40324-014-0012-y>.
- [S17] J. Fuchsberger, P. Aigner, G. Haase, S. Niederer, H. Schima, G. Plank, and E. Karabelas. On the incorporation of obstacles in a fluid flow problem using a navier-stokes-brinkman penalization approach, 2021.

- [S18] E. Haines. Point in polygon strategies. In *Graphics Gems*, pages 24–46. Elsevier, 1994. URL <https://doi.org/10.1016/b978-0-12-336156-1.50013-6>.
- [S19] V. E. Henson and U. M. Yang. BoomerAMG: A parallel algebraic multigrid solver and preconditioner. *Applied Numerical Mathematics*, 41(1):155–177, Apr. 2002. URL [https://doi.org/10.1016/s0168-9274\(01\)00115-5](https://doi.org/10.1016/s0168-9274(01)00115-5).
- [S20] C. Hirt, A. Amsden, and J. Cook. An arbitrary lagrangian-eulerian computing method for all flow speeds. *Journal of Computational Physics*, 14(3):227–253, Mar. 1974. URL [https://doi.org/10.1016/0021-9991\(74\)90051-5](https://doi.org/10.1016/0021-9991(74)90051-5).
- [S21] S. Hodis, S. Uthamaraj, A. L. Smith, K. D. Dennis, D. F. Kallmes, and D. Dragomir-Daescu. Grid convergence errors in hemodynamic solution of patient-specific cerebral aneurysms. *Journal of Biomechanics*, 45(16):2907 – 2913, 2012. ISSN 0021-9290. doi: <https://doi.org/10.1016/j.jbiomech.2012.07.030>.
- [S22] T. J. Hughes, W. K. Liu, and T. K. Zimmermann. Lagrangian-eulerian finite element formulation for incompressible viscous flows. *Computer Methods in Applied Mechanics and Engineering*, 29(3):329–349, Dec. 1981. URL [https://doi.org/10.1016/0045-7825\(81\)90049-9](https://doi.org/10.1016/0045-7825(81)90049-9).
- [S23] K. E. Jansen, C. H. Whiting, and G. M. Hulbert. A generalized- $\alpha$  method for integrating the filtered navier–stokes equations with a stabilized finite element method. *Computer Methods in Applied Mechanics and Engineering*, 190(3-4):305–319, Oct. 2000. URL [https://doi.org/10.1016/s0045-7825\(00\)00203-6](https://doi.org/10.1016/s0045-7825(00)00203-6).
- [S24] Y. Jin, S. Chai, J. Duffy, C. Chin, and N. Bose. Urans predictions of wave induced loads and motions on ships in regular head and oblique waves at zero forward speed. *Journal of Fluids and Structures*, 74:178 – 204, 2017. ISSN 0889-9746. doi: <https://doi.org/10.1016/j.jfluidstructs.2017.07.009>.
- [S25] V. John and E. Schmeyer. Finite element methods for time-dependent convection–diffusion–reaction equations with small diffusion. *Computer Methods in Applied Mechanics and Engineering*, 198(3-4):475–494, Dec. 2008. URL <https://doi.org/10.1016/j.cma.2008.08.016>.
- [S26] E. Karabelas, M. A. F. Gsell, C. M. Augustin, L. Marx, A. Neic, A. J. Prassl, L. Goubergrits, T. Kuehne, and G. Plank. Towards a computational framework for modeling the impact of aortic coarctations upon left ventricular load. *Frontiers in Physiology*, 9, May 2018. URL <https://doi.org/10.3389/fphys.2018.00538>.
- [S27] E. Karabelas, G. Haase, G. Plank, and C. M. Augustin. Versatile stabilized finite element formulations for nearly and fully incompressible solid mechanics. *Computational Mechanics*, 65(1):193–215, Sept. 2019. URL <https://doi.org/10.1007/s00466-019-01760-w>.
- [S28] D. Kuzmin. Explicit and implicit FEM-FCT algorithms with flux linearization. *Journal of Computational Physics*, 228(7):2517–2534, Apr. 2009. URL <https://doi.org/10.1016/j.jcp.2008.12.011>.
- [S29] D. Kuzmin and M. Möller. Algebraic flux correction i. scalar conservation laws. In *Flux-Corrected Transport*, pages 155–206. Springer-Verlag, 2008. URL [https://doi.org/10.1007/3-540-27206-2\\_6](https://doi.org/10.1007/3-540-27206-2_6).

- [S30] C. C. Long, M. Esmaily-Moghadam, A. L. Marsden, and Y. Bazilevs. Computation of residence time in the simulation of pulsatile ventricular assist devices. *Computational Mechanics*, 54(4):911–919, sep 2013. URL <https://doi.org/10.1007/s00466-013-0931-y>.
- [S31] P. W. Longest and S. Vinchurkar. Effects of mesh style and grid convergence on particle deposition in bifurcating airway models with comparisons to experimental data. *Medical Engineering & Physics*, 29(3):350 – 366, 2007. ISSN 1350-4533. doi: <https://doi.org/10.1016/j.medengphy.2006.05.012>.
- [S32] L. Marx, M. A. Gsell, A. Rund, F. Caforio, A. J. Prassl, G. Toth-Gayor, T. Kuehne, C. M. Augustin, and G. Plank. Personalization of electro-mechanical models of the pressure-overloaded left ventricle: Fitting of Windkessel-type afterload models: Fitting of Windkessel afterload models. *Philos. Trans. R. Soc. A Math. Phys. Eng. Sci.*, 378(2173), 2020. ISSN 1364503X. URL <https://doi.org/10.1098/rsta.2019.0342>.
- [S33] M. E. Moghadam, , Y. Bazilevs, T.-Y. Hsia, I. E. Vignon-Clementel, and A. L. Marsden. A comparison of outlet boundary treatments for prevention of backflow divergence with relevance to blood flow simulations. *Computational Mechanics*, 48(3):277–291, Apr. 2011. URL <https://doi.org/10.1007/s00466-011-0599-0>.
- [S34] T. Möller and B. Trumbore. Fast, minimum storage ray-triangle intersection. *Journal of Graphics Tools*, 2(1):21–28, Jan. 1997. URL <https://doi.org/10.1080/10867651.1997.10487468>.
- [S35] A. Neic, M. A. Gsell, E. Karabelas, A. J. Prassl, and G. Plank. Automating image-based mesh generation and manipulation tasks in cardiac modeling workflows using meshtool. *SoftwareX*, 11:100454, Jan. 2020. URL <https://doi.org/10.1016/j.softx.2020.100454>.
- [S36] L. H. Pauli. *Stabilized Finite Element Methods for Computational Design of Blood-Handling Devices*. PhD thesis, 6 2016.
- [S37] S. B. Pope. Ten questions concerning the large-eddy simulation of turbulent flows. *New Journal of Physics*, 6:35–35, Mar. 2004. URL <https://doi.org/10.1088/1367-2630/6/1/035>.
- [S38] N. Scuro, E. Angelo, G. Angelo, and D. Andrade. A cfd analysis of the flow dynamics of a directly-operated safety relief valve. *Nuclear Engineering and Design*, 328:321 – 332, 2018. ISSN 0029-5493. doi: <https://doi.org/10.1016/j.nucengdes.2018.01.024>.
- [S39] O. Steinbach. *Numerical approximation methods for elliptic boundary value problems: finite and boundary elements*. Springer Science & Business Media, 2007.
- [S40] P. L. Tallec and J. Mouro. Fluid structure interaction with large structural displacements. *Computer Methods in Applied Mechanics and Engineering*, 190(24-25):3039–3067, Mar. 2001. URL [https://doi.org/10.1016/s0045-7825\(00\)00381-9](https://doi.org/10.1016/s0045-7825(00)00381-9).
- [S41] E. Vigmond, R. W. dos Santos, A. Prassl, M. Deo, and G. Plank. Solvers for the cardiac bidomain equations. *Progress in Biophysics and Molecular Biology*, 96(1-3):3–18, Jan. 2008. URL <https://doi.org/10.1016/j.pbiomolbio.2007.07.012>.

- [S42] E. J. Vigmond, M. Hughes, G. Plank, and L. Leon. Computational tools for modeling electrical activity in cardiac tissue. *Journal of Electrocardiology*, 36:69–74, Dec. 2003. URL <https://doi.org/10.1016/j.jelectrocard.2003.09.017>.
- [S43] S. T. Zalesak. Fully multidimensional flux-corrected transport algorithms for fluids. *Journal of Computational Physics*, 31(3):335–362, June 1979. URL [https://doi.org/10.1016/0021-9991\(79\)90051-2](https://doi.org/10.1016/0021-9991(79)90051-2).